Subsurface deposition of Cu-rich massive sulfide underneath a Palaeoproterozoic seafloor hydrothermal system – The Red Bore prospect, Western Australia

Agangi, A.[1], Reddy, S.M. [1], Plavsa, D. [1], Vieru, C. [2], Selvaraja, V. [3], LaFlamme, C. [3], Jeon, H. [4], Martin, L. [4], Nozaki, T. [5], Takaya, Y.[6], Suzuki, K.[5]

[1] Department of Applied Geology, Curtin University, Bentley 6012 WA, Australia

[2] Thundelarra Ltd., 186 Hampden Road Nedlands, 6009 WA, Australia

[3] Centre for Exploration Targeting (CET), University of Western Australia, 35 Stirling Highway, Crawley 6009 WA, Australia

[4] Centre for Microscopy, Characterisation and Analysis (CMCA), University of Western Australia, 35 Stirling Highway, Crawley 6009 WA, Australia

[5] Research and Development (R&D) Center for Submarine Resources, Japan Agency for Marine-Earth Science and Technology (JAMSTEC), 2-15 Natsushima-cho, Yokosuka, Kanagawa 237-0061, Japan

[6] Department of Resources and Environmental Engineering, School of Creative Science and Engineering, Waseda University, 3-4-1 Okubo, Shinjuku-ku, Tokyo 169-8555, Japan

Abstract

The Proterozoic Bryah and Yerrida basins of Western Australia contain important base and precious metal deposits. Here we present microtextural data, trace element and S isotope analyses of massive sulfide mineralisation hosted in Palaeoproterozoic subvolcanic rocks (dolerite) recently discovered at Red Bore. The small-scale high-grade mineralisation, which extends from the sub-surface to at least 95 m down-hole, is dominated by massive chalcopyrite and contains minor pyrite and Bi-Te-(Se) phases. Massive sulfide mineralisation is surrounded by discontinuous brecciated massive magnetite, and a narrow (<2 m) alteration halo, which suggests very focussed fluid flow. Laser ablation ICP-MS analyses indicate that chalcopyrite contains up to 10 ppm Au and in excess of 100 ppm Ag. Sulfur isotope analyses of pyrite and chalcopyrite indicate a narrow range of $\delta^{34}S_{VCD}$ (-0.2 to +4.6 ‰), and no significant mass-independent fractionation ($-0.1 < \Delta^{33}S < +0.05$ ‰). Re-Os isotope analyses yield scattered values, which suggests secondary remobilisation. Despite the geographical proximity and the common Cu-Au-Ag association, the mineralisation at Red Bore has significant differences with massive sulfide mineralisation at neighbouring DeGrussa, as well as other massive sulfide deposits around the world. These differences include the geometry, sub-volcanic host rocks, extreme Cu enrichment and narrow $\delta^{34}S$ ranges. Although a possible explanation for some of these characteristics is leaching of S and metals from the surrounding volcanic rocks, we favour formation as a result of the release of a magmatic fluid phase along very focussed pathways, and we propose that mixing of this fluid with circulating sea water contributed to sea floor mineralisation similar to neighbouring VHMS deposits. Our data are permissive of a genetic association of Red Bore mineralisation with VHMS deposits nearby, thus suggesting a direct connection between magmatism and mineralising fluids responsible for VHMS deposition at surface. Therefore, the Red Bore mineralisation may represent the magmatic roots of a VHMS system.

Introduction

Volcanic-hosted massive sulfide (VHMS) deposits are the source of significant amounts of Cu, Zn, Pb, Ag and Au (Large 1992; Galley et al. 2007). These deposits form in submarine environments, at both extensional and convergent margin settings (Yeats et al. 2014; Huston et al. 2010; Galley et al. 2007; Binns et al. 2007), where convective sea water circulation, driven by magma intrusion at shallow crustal depths, deposits metals when these heated fluids are discharged back into sea water (Ohmoto 1996; Ross and Mercier-Langevin 2014). VHMS deposits occur discontinuously throughout Earth's history from the Archaean to the Phanerozoic (Huston et al. 2010; Sharpe and Gemmell 2002) and are considered to be the fossilised equivalents of present day massive sulfides deposited at the emergence of submarine hydrothermal systems (de Ronde et al. 2005; Hannington 2014; Petersen et al. 2014).

This mechanism of ore deposition implies two end members for the source of metals: the country rocks (including sediments, volcanic rocks and the basement) and the magma that drives convective circulation. The leaching of country rocks by circulating sea water is a widely accepted mechanism as a source of metals, for example in Kuroko-type VHMS deposits (Ohmoto 1996). More recently, substantial evidence has emerged pointing to a significant magmatic contribution for both fluids and metals in ancient and present day systems (Huston et al. 2011; Moss et al. 2001; Gemmell et al. 2004). Sea water involvement in the deposition of VHMS mineralisation is indicated by: 1) low, sea water-like salinity of fluid inclusions (5 – 6 wt% Na_{eq} on average; Peter et al. 2007), although high-salinity brines and vapours have been observed in some modern vents and ancient VHMS deposits (Shanks III 2001; Solomon et al. 2004), likely due to phase separation; 2) $\delta^{18}O$ (> 5 ‰) and $\delta^{34}S$ of sulfate minerals indicating equilibrium with sea water at the time of deposition (de Ronde et al. 2014); 3) O and H isotope composition of alteration minerals associated with sea water interaction with hot magmatic rocks (Shanks III 2001; Shanks III and Thurston 2012) and of fluids

64 emitted at present-day submarine centres (de Ronde et al. 2005); and 4) in the specific case of
65 Archaean VHMS deposits, multiple S isotope signatures of sulfide minerals yielding $\Delta^{33}S < 0$, implying
66 sourcing of S from Archaean sea water sulfate (Farquhar et al. 2011; Bekker et al. 2009; Chen et al.
67 2015). On the other hand, studies of volcanic rocks associated with VHMS deposits (Timm et al.
68 2012; Moss et al. 2001) and melt inclusions in unmineralised rocks from the Manus basin
69 (Kamenetsky et al. 2001; Yang and Scott 1996) have shown that magmas are potential sources of
70 metals in this type of deposits. A magmatic involvement is expected to be reflected in geochemical
71 and isotopic compositions of some VHMS deposits, such as enrichment of Cu-Au-Ag-Bi-Se,
72 intermediate to high-sulfidation assemblages, high fluid $\delta^{18}O$, narrow $\delta^{34}S$ ranges and aluminous
73 alteration (Peter et al. 2007; Huston et al. 2011). However, it is difficult to determine whether these
74 observations are the result of magmatic-hydrothermal fluid input or leaching of volcanic rocks by sea
75 water-derived fluids.

76 Here, we present textural and mineralogical observations, trace element and S isotope
77 compositions of recently discovered mineralisation, called the Red Bore prospect of central Western
78 Australia (Fig 1) and evaluate its formation in the light of the previous discussion. This mineralisation
79 includes pipe-like massive chalcopyrite ore spatially related to VHMS deposits hosted in a
80 Palaeoproterozoic mafic volcanic succession. The geometry and the very Cu-rich composition set this
81 mineralisation apart from VHMS mineralisation at the district scale.

82 **Geological setting**

83 Regional geology

84 Sulfide mineralisation at Red Bore is hosted by the mafic igneous rocks of the Narracoota
85 Formation within the Bryah Basin (Fig. 1). The volcano-sedimentary Bryah and Padbury Groups were
86 deposited along the northern margin of the Yilgarn Craton between 2000 and 1800 Ma (Occhipinti et

al. 1998a; 2004; Pirajno and Occhipinti 2000) and are interpreted to have formed on a continental margin or in a rift setting (Occhipinti et al. 1998a; Pirajno et al. 1998, 2004; Pirajno and Occhipinti 2000). A recent model proposed that extension was preceded by upwelling caused by the impingement of a mantle plume (Pirajno et al. 2016). The Karalundi Formation is the lowest unit of the Bryah Basin and includes a clastic sedimentary succession (conglomerate, wacke, siltstone, black shale) and mafic volcanic rocks (Pirajno and Occhipinti 2000). The Narracoota Formation overlies the Karalundi Formation and forms a predominant proportion of the succession in the Bryah Basin. It is composed of voluminous mafic to ultramafic volcanic rocks, and intrusive rocks. The mafic rocks contain pillow basalt, hyaloclastite basalt, sheeted dykes, a layered mafic-ultramafic igneous complex and minor felsic rocks, and show evidence for sea floor metasomatism in the form of tremolite-talc-chlorite-bearing assemblages (Pirajno and Occhipinti 2000; Pirajno et al. 1998, 2000; Occhipinti et al. 2004). The Narracoota Formation is overlain by metasediments of the Ravelstone Formation and Horseshoe Formation, which include wacke, shale, siltstone, chert and banded iron formation (Pirajno et al. 2000). Rocks of the Bryah Group have undergone multiple stages of deformation and greenschist facies metamorphism during formation of the Capricorn Orogen in the Proterozoic (Pirajno et al. 1998; Hynes and Gee 1986; Reddy and Occhipinti 2004).

Sediments and mafic rocks associated with the Karalundi and Narracoota formations contain Cu-Au-Ag VHMS deposits at DeGrussa and Horseshoe Lights and the high-grade Monty deposit (Pirajno et al. 2000; Hawke et al. 2015b; Sandfire Resources Report, 2016). The Cu-Au-Ag DeGrussa deposit is mostly hosted in turbiditic sedimentary rocks, and consists of four steeply dipping lensoid ore lodes separated from each other by two large faults, with a combined strike length of 800 m. Due to deformation related to the Jenkin fault (Fig. 1) and the lack of outcrop, the stratigraphic relationships between DeGrussa and Red Bore are not clear in the field. The stratabound sulfides at DeGrussa are massive, fine-grained and consist of pyrite, chalcopyrite, and pyrrhotite with lesser sphalerite, galena, marcasite, and molybdenite. Chalcocite, malachite, azurite, chrysocolla, cuprite

and native copper are present in the supergene ore zone. VHMS mineralisation at DeGrussa has recently been dated at 2027 – 2011 Ma (Re-Os on molybdenite) and 2040 – 2030 Ma (Pb-Pb on galena modelled according to Stacey and Kramers, 1975), an age overlapping with the age of volcanism (Hawke et al. 2015b). Total estimated resources at April 2016 are 10.7 Mt of ore containing 4.5 % Cu and 1.8 g/t Au (Sandfire Resources Report, 2016). The Monty deposit is composed of chalcopyrite, pyrite and pyrrhotite with minor sphalerite and galena, and contains resources of 700,000 tonnes at approximately 10 % Cu and 2 g/t Au (Sandfire Resources Report, 2016).

Drill core description

Surface expression of Red Bore mineralisation is represented by the presence of a gossan and a geographically restricted magnetic anomaly (Fig. 1B). Closely-spaced drilling (more than30 drill holes, a few m to a few tens of m apart) carried out by Thundelarra Ltd. has intersected steeply-dipping elongate mineralisation containing massive chalcopyrite and massive magnetite. The mineralisation does not extend along strike, suggesting a “pipe-like”, rather than tabular geometry. Double intersections may indicate the presence of two separate mineralised bodies or tectonic duplication. Drill core lithology is dominated by dolerite, coarse (mm-scale)-grained massive mafic rocks (gabbro, ultramafic rocks), mafic volcanic and volcaniclastic rocks (lava and possibly hyaloclastite), and fine-grained, finely-bedded sedimentary rocks. Mineralisation is largely hosted in mafic rocks (mostly dolerite) of the Narracoota Formation and to a lesser extent, by sedimentary rocks. The mineralisation extends from the near-surface (shallowest intersection at 6 m depth) to at least ~100 m (Fig. 1C). The mineralisation is open at depth, and its total extent is not known.

In several samples, the volcanic-intrusive host rocks show signs of semi-brittle deformation. The mineralisation is surrounded by a narrow (<2 m wide) alteration zone represented in core samples by a fine-grained “bleached” pale green rock mostly composed of talc, carbonate, chlorite

and silica. There is no evidence of a hydrothermal system (veins) developed around the mineralisation, as veins were not intersected outside the mineralised zone.

Analytical techniques

Samples collected during this study were analysed using scanning electron microscopy, whole-rock geochemistry, laser-ablation inductively-coupled plasma mass spectrometry, secondary ion mass spectrometry for multiple S isotopes and negative thermal ionisation mass spectrometry for Re-Os isotopes. Analytical methods are presented in ESM E-1.

Sample description

Drill core description

The cores have intersected mineralisation for a length of up to 10 – 12 m and show a zoned distribution of minerals, with a massive chalcopyrite zone (up to 7 m) in the centre and a discontinuous massive magnetite zone at the margin (see ESM E-2 for drill hole locations and orientation). The central ore zone (Fig. 2A) is composed of massive chalcopyrite (>90 %; for example, a 7.05 m intersection at 28.4 wt% Cu, 1.3 ppm Au and 32 ppm Ag was found in drill core TRBDD09) with needle-like silicate inclusions, pyrite and minor covellite [CuS]. The marginal zone is composed of massive magnetite (>90 %) with minor chalcopyrite and pyrite, and carbonate-rich veinlets (Fig. 2B). The mineralisation is oxidised in the top 25 m, and contains Fe- and Cu-oxy-hydroxides. In addition, disseminated pyrite and chalcopyrite are hosted by finely-bedded sedimentary rocks in the southwestern part of the tenement.

The massive magnetite is brecciated in places, forming a monomictic matrix-supported chaotic breccia (Fig. 2B). Clasts of this breccia are mostly angular, up to ~10 cm in size, composed of magnetite-replaced mafic rocks, and are cross-cut by brown carbonate veinlets. These veinlets do

not cross-cut the surrounding matrix. The matrix has a grain size of up to a few mm and is composed of magnetite and silicate minerals. Cement between clasts could not be identified from hand specimens. Minor sulfide veinlets (chalcopyrite in particular) cross-cut both the matrix and the clasts (Fig. 2C).

Microtextures

Massive chalcopyrite ore contains abundant elongate silicate inclusions, such as amphibole and talc, which have been variably silicified (Fig. 3A). These silicate inclusions are distributed along planes, thus defining a foliation, although individual crystals are randomly oriented, and are interpreted as hydrothermal. Sulfidation of silicate needles can be observed in some cases, whereby chalcopyrite or pyrite form µm-scale grains on previous silicates (Fig. 3B). Samples of massive magnetite are non-foliated and composed of sub-round magnetite grains, up to 100 µm in size, which are partly rimmed by haematite. Massive magnetite samples contain chalcopyrite and pyrite occurring as mm- to sub-mm-scale veinlets or as interstitial grains (Fig. 3C). In addition, magnetite is cross-cut by Fe-carbonate veinlets that also contain Ca-amphibole and minor sulfide phases (chalcopyrite, sphalerite, Co-sulfide) (Fig. 3D). Semi-quantitative EDS analyses indicate that sphalerite contains up to 7.5 wt% Fe.

Pyrite occurs in both massive chalcopyrite and massive magnetite samples as anhedral grains and veinlets with an apparent "cleaved" texture (Fig. 3B). EDS semi-quantitative analyses indicate the presence of variable amounts of Co and high-magnification SEM images suggest a nanoscale granular texture. This pyrite may by the product of sulfidation of a silicate (e.g. amphibole). Bismuth-Te-Se phases, in some cases coexisting with a Te-Ag phase (Fig. 3B-E), occur either as inclusions up to 50 – 60 µm in size or along µm-scale veinlets in pyrite and chalcopyrite. These Bi-Te-Se grains contain between ~24 – 41 wt% Te, and ~5 and 10 wt% Se (EDS). Anhedral S-Co-O-Si grains that show zoned texture in BSE images occur in both massive chalcopyrite and massive magnetite samples. X-

ray element maps of these grains indicate that S, Cu and Co (up to 35 wt%) are enriched at the margins and along cracks, whereas Si and O contents decrease towards grain margins and cracks (Fig. 3F), thus indicating replacement of a silicate mineral. Copper sulfide (~$CuS_{0.9}$ covellite, of likely supergene origin) occurs as anhedral, cracked grains in massive chalcopyrite. The alteration halo around mineralisation contains Mg-Fe silicate (Fe-bearing talc, or minnesotaite), Si, Ca-Fe-carbonate, Ca-(±K)-bearing amphibole and chlorite. Semi-quantitative EDS analyses indicate that this amphibole contains 11 – 21 wt% CaO and Mg/(Mg+Fe) = 0.41 – 0.71.

Analytical results

Bulk assays

Bulk assays indicate contents of Cu from 0.03 to 30.1 wt%, Au up to 20 ppm and Ag up to 40 ppm (Fig. 4). Copper concentrations have a broad positive correlation with Au and Ag, although some analyses have distinctively high Au and Ag and relatively low Cu (Au/Cu $\times$ 10000 ≥5). There is also a broad negative correlation between Au/Cu and Ag, indicating that the highest Au/Cu values are found in moderately chalcopyrite-rich samples.

Mineral chemistry (LA-ICP-MS)

Chalcopyrite contains up to ~8 ppm Au and up to 240 ppm Ag (Fig. 5, ESM Table 1). The highest Au and Ag concentrations were measured in chalcopyrite veinlets emplaced at the margin of the mineralised body (sample TRBDD08 51.7 m). Tellurium is mostly <10 ppm and Bi <30 ppm in both chalcopyrite and pyrite, although the presence of Bi-Te±Se inclusions resulted in significantly higher concentrations (Bi and Te up to more than 1000 ppm) and positive correlations between these elements in some spot analyses. Selenium content (mostly ~100 – 1200 ppm in chalcopyrite) is strongly variable between samples but has narrow ranges within samples and between minerals of the same samples (Fig. 5). Plots of signal intensity as counts per second (cps) versus analysis time (s)

confirm the presence of various inclusions of Bi-Te±Se and Te±Ag±Au phases in both chalcopyrite and pyrite (Fig. 6). Selenium concentrations are only partly controlled by inclusions.

Chalcopyrite contains higher Zn and Sn concentrations (~10 to 740 ppm Zn) than other minerals (pyrite contains <50 ppm Zn). Molybdenum concentrations of chalcopyrite at the margin of the ore body (TRDCC09 35.5 m) are higher and more variable (Mo ~1 – 80 ppm) than those from the centre (Fig. 5). Pyrite is the main carrier of Ag (~300 – 600 ppm), Pb (~30 – 700 ppm), Tl (~1 – 15 ppm), Cr and Re (up to ~3 and 1.4 ppm, respectively), and has low concentrations of As and Sb (< 20 ppm and <1 ppm, respectively). Magnetite has low concentrations of Ti (<70 ppm), V (<60 ppm) and Ni (up to 30 ppm) and overlaps with magnetite from banded iron formation and metamorphic magnetite in the discrimination plots of (Nadoll et al. 2014) (Fig. 7). However, manganese (up to 2500 ppm Mn) is higher than hydrothermal magnetite, and similar to magmatic magnetite from mafic rocks (Dare et al. 2014). The Cu content of magnetite is between 50 and 2600 ppm (omitting a few higher outlying values likely due to chalcopyrite inclusions), and Sn is between 1 and 10 ppm.

Values of $^{208}Pb/^{206}Pb$ and $^{207}Pb/^{206}Pb$ of chalcopyrite and pyrite measured by LA-ICP-MS during trace element analysis span a wide range ($^{208}Pb/^{206}Pb$ ~ 0.48 – 2.30), and define a linear trend in the $^{208}Pb/^{206}Pb$ vs. $^{207}Pb/^{206}Pb$ plot (ESM Fig. 1). The highest values of $^{208}Pb/^{206}Pb$ and $^{207}Pb/^{206}Pb$ overlap with values expected from Palaeoproterozoic crust according to the model of Stacey and Kramers (1975). Disseminated chalcopyrite and pyrite largely overlap with $^{208}Pb/^{206}Pb$ and $^{207}Pb/^{206}Pb$ measured at DeGrussa (Hawke et al. 2015b; Belousov et al. 2016). Overall the values define a rather continuous trend, but spot analyses of sulfides forming veinlets in massive magnetite samples have more radiogenic (lower) values of $^{208}Pb/^{206}Pb$ and $^{207}Pb/^{206}Pb$ in comparison with analyses from massive and, especially, disseminated mineralisation.

In situ S isotope analyses (SIMS)

Multiple S isotopes (^{32}S, ^{33}S and ^{34}S) of chalcopyrite and pyrite were analysed in eight samples collected at down-hole depths between 31.5 and 66.0 m from five cores. Chalcopyrite and pyrite yielded $\delta^{34}S$ between +1.12 and +4.63 ‰, and $\delta^{34}S$ values between -0.27 and +4.19 ‰, respectively (Fig. 8, ESM Table 2). However, most analyses of both pyrite and chalcopyrite (> 80 % of the 87 spots) yielded $\delta^{34}S$ values between +3.0 and +4.6 ‰ (Fig 8). Values of $\delta^{34}S$ below +3.0 ‰ are mostly scattered, and lie up to 2 ‰ lower than other analyses in the same sample (Fig 8B). If these outlying analyses are excluded, ranges of $\delta^{34}S$ in single samples are extremely narrow (≤1 ‰). Variations of $\delta^{34}S$ between samples do not correlate with sampling depth or sample texture (i.e. massive or veinlets). In samples where both phases were analysed, chalcopyrite tends to have slightly higher $\delta^{34}S$ values than pyrite (~0.5 – 0.8 ‰ on average, greater than the $\delta^{34}S$ 2σ error of 0.33 ‰ for chalcopyrite). Deviations from mass-dependent fractionation are not significant ($-0.1 < \Delta^{33}S < +0.05$ ‰).

Re-Os isotope analyses

The samples have Re and Os contents of 6.20 – 99.6 ppb and 59.5 – 1030 ppt, respectively. $^{187}Re^{188}/Os$ ratios are between 1770 and 57900, and have a broad positive correlation with $^{187}Os/^{188}Os$ ratios. The regression on all ten analyses gives a very poor age of 1030 ± 170 Ma (MSWD of 9050) and a meaningless negative initial $^{187}Os/^{188}Os$ of -45. A regression on six out of ten analyses (excluding samples BM002185 and BM002188) yielded a marginally improved age of 959 ± 110 Ma (MSWD of 50), and an initial $^{187}Os/^{188}Os$ of 40 (ESM Fig. 2).

Discussion

Sulfide deposition from a magmatic fluid at Red Bore? Geologic, elemental and isotopic evidence

In VHMS deposits, elemental and isotopic data of the ore and associated alteration have been used to support either derivation of metals from sea water leaching of surrounding rocks or

derivation from magmas. However, these data can be equivocal as “magmatic” signatures may be acquired either by direct magmatic-hydrothermal input or by leaching of volcanic rocks by circulating sea water (Huston et al. 2011; Urabe and Marumo 1991). Therefore, the role of magmatic fluids in the formation of VHMS mineralisation can be better evaluated based on a combination of factors, including deposit- to micro-scale geological and textural observations, mineral associations and geochemical data. For example, in VHMS systems associated with felsic magmatism, the spatial association of VHMS mineralisation with intrusions (Galley 2003) and with aluminous, advanced argillic alteration, similar to alteration typically associated with porphyry style deposits (e.g. at Mt Lyell; Large et al. 1996) has been used to infer a causative relationship between granitic magmatism and mineralisation. In contrast to these felsic-associated systems, talc-carbonate-silica-amphibole alteration assemblages at Red Bore resemble those found in mafic-hosted sea floor hydrothermal systems. In mafic volcanic-hosted VHMS deposits of Cyprus, typical alteration assemblages are dominated by quartz and chlorite, replacement of feldspar, with local epidote and haematitic jasper (Adamides 2010). These deposits show evidence of deposition both at the surface (exhalative) and in the subsurface. Most deposits occur along faults, and mineralisation textures indicate replacement of host rocks (Adamides 2010). At Rudny-Altai, where Besshi-style deposits hosted in mafic igneous and sedimentary rocks have been recognised, the alteration assemblage is dominated by amphibole (anthophyllite), chlorite and quartz (Lobanov et al. 2014).

The enrichment in Cu, Au and Ag is typical of VHMS deposits associated with mafic volcanic rocks, either Cyprus/Besshi-types (Galley et al. 2007; Adamides 2010), or mid-oceanic ridge style (Murphy and Meyer 1998). High concentrations of these elements may indicate a magmatic association even in other types of VHMS deposits. For example, after reviewing radiogenic and stable isotope data on Kuroko-type deposits, Urabe and Marumo (1991) concluded that most Cu is of magmatic origin. In contrast, Ohmoto (1996) attributed most metals to leaching of host lithologies by circulating sea water derived fluids. The tendency of Cu and other chalcophile elements, such as

276 Au and Ag, to partition into magmatic fluids coexisting with silicate melts is well-reported
277 (Lowenstern et al. 1991; Heinrich et al. 1992). For example, in mafic magmas of the Manus basin, a
278 sudden decrease of Cu and Au during fractionation has been interpreted as evidence of loss of these
279 elements to an exsolving S-rich volatile phase (Sun et al. 2004). Magmatic vapours derived from
280 mafic magmas tend to be Cu-rich and Cu-phases such as chalcocite (Cu_2S), covellite (CuS) and
281 chalcopyrite have been found as incrustations formed by these fluids at volcanic vents or trapped as
282 fluid inclusions in phenocrysts (Simon and Ripley 2011; Agangi and Reddy 2016). In modern
283 submarine hydrothermal systems, several studies suggest that magmatic volatiles are likely
284 responsible for the transport and deposition of metals such as Cu and Au and other chalcophile
285 elements (de Ronde et al. 2005, 2014; Berkenbosch et al. 2012; Petersen et al. 2014). High Se
286 contents in VHMS deposits are also considered as indicative of derivation from a magmatic source
287 (Hannington 2014), although others have proposed that Se could be sourced from black shales
288 (Layton-Matthews et al. 2008). Selenium concentrations in pyrite and chalcopyrite at Red Bore and
289 at DeGrussa are high in comparison with other VHMS deposits in Western Australia (Belousov et al.
290 2016), which may provide further indications of a magmatic input. Similar high Se values have been
291 measured in bulk samples of ultramafic-hosted VHMS (Murphy and Meyer 1998) and in single sulfide
292 phases from mafic-ultramafic modern VHMS deposits (Wohlgemuth-Ueberwasser et al. 2015) (Fig.
293 9).

294 Bi-Te-(Se) phases have only in some cases been described in VHMS deposits, as occurring in
295 the deep portion of deposits (Cu-rich stringer zone) in the Iberian Pyrite Belt (Marcoux et al. 1996)
296 and Jabal Sayid deposit of Saudi Arabia (Sabir 1979) or in sulfide chimneys (Maslennikov et al. 2013;
297 Berkenbosch et al. 2012). Besides VHMS deposits, Bi-Te phases have been reported in
298 orthomagmatic, skarn, porphyry and epithermal deposits, where they form compounds with Au, Ag,
299 Pt group elements and other precious metals (Ciobanu et al. 2005, 2006; Cook et al. 2009; Dora et al.
300 2014). Te-Bi-(Au) phases are also known to be deposited from high-temperature volcanic gases

301 (Symonds et al. 1987; Henley et al. 2012), and Te intake in chalcopyrite is believed to be enhanced at
302 high temperature (Hannington et al. 1991). Therefore, Te, Bi, Se and Au, as a suite are compatible
303 with a magmatic-hydrothermal derivation and have been proposed as being indicative of a
304 magmatic source (Galley et al. 2007; Berkenbosch et al. 2012; Lehmann et al., 2013).

305 Values of $\delta^{34}S$ in VHMS deposits overall span a wide range (Hannington 2014; Lobanov et al.
306 2014). The fact that many VHMS deposits contain sulfates with $\delta^{34}S$ that mirrors the $\delta^{34}S$ of sea
307 water at the time of deposition is good evidence for direct involvement of sea water sulfate (Huston
308 et al. 2010). However, VHMS hosted in mafic-dominated volcano-sedimentary successions tend to
309 have narrow ranges of $\delta^{34}S$ (Besshi-type ~ 0 – 4 ‰, Fig. 8) in comparison with felsic volcanic-hosted
310 VHMS deposits, which have higher and more varied S isotope compositions (Lydon 1984; Petersen et
311 al. 2014; Hannington 2014; Cloutier et al. 2015). Vent fluids discharged at sediment-poor mid-ocean
312 ridges also tend to have narrow $\delta^{34}S$ ranges (between 0 and 6 ‰; Marini et al. 2011). In sulfide-poor
313 mafic complexes, such as the Merensky Reef of the Bushveld Complex or the Stillwater Complex, for
314 which the S may have been accommodated by the melt, rather than incorporated from country
315 rocks, sulfides have similar compositions, $\delta^{34}S$ = 0 – 4 ‰ (Ripley and Li 2003) (Fig. 8). The
316 homogeneity of most $\delta^{34}S$ values (80 % of analyses are between +3.0 to +4.6 ‰, Fig. 8) of
317 chalcopyrite and pyrite at Red Bore is consistent with precipitation from a homogenous (one-phase)
318 fluid of magmatic origin. Precipitation of chalcopyrite from H_2S is expected to cause relatively minor
319 fractionation of S isotopes ($\delta^{34}S$ variation <1 ‰; Kajiwara and Krouse 1971). Thermochemical sulfate
320 reduction results in strong fractionation between sulfate and sulfide ($\delta^{34}S$ sulfate - $\delta^{34}S$ sulfide = 17
321 ‰ at temperatures of 300 – 350°C, relevant for Red Bore; Ohmoto 1986). Assuming a
322 Palaeoproterozoic sea water sulfate $\delta^{34}S$ value of ~20 ‰ (Farquhar et al. 2011, ESM Fig. 3), sulfide
323 originated through this mechanism would have $\delta^{34}S$ = 3 – 20 ‰, depending on the proportion of
324 sulfate reduced. However, the fact that no sulfate was found at Red Bore may indicate that the fluids
325 were relatively reduced and sulfate was not the dominant species in the mineralising fluids (Murphy

and Meyer 1998). Biogenic sulfate reduction produces sulfide with strongly negative $\delta^{34}S$ (≥-30 ‰). Thus, the absence of $\delta^{34}S < 0$ ‰ in our samples is not compatible with such processes. Further, the absence of mass-independent fractionation of S isotopes excludes the possibility that sedimentary S may have been remobilised from surrounding Archaean terrains (Bekker et al. 2009).

The slightly lower and scattered $\delta^{34}S$ measured in some of our analyses ($\delta^{34}S$ ~<2.5 ‰) may be due to minor events of phase separation in the mineralising fluid. Vapour separation is associated with partial oxidation of S to form SO_4^{-2} (Drummond and Ohmoto 1985) according to the equation $H_2S\ (aq) + 4H_2O \rightarrow SO_4^{2-}(aq) + 2H^+ + 4H_2(g)$. Separation of a SO_4^{2-}-rich vapour would have preferentially extracted heavy S isotopes, imparting lower $\delta^{34}S$ values to the remaining fluid. This may have occurred locally during transient pressure release due to, for instance, tectonic movements. However, later remobilisation processes related with the long and complex tectonic history of the basin cannot be excluded.

Secondary remobilisation revealed by Re-Os and Pb-Pb isotopes

Given the scatter of Re-Os isotope values, we do not attribute any specific geochronological meaning to these analyses. The Re-Os data indicate Re and Os remobilisation during the complex tectonic history of the area. The linear trend observed in plots of Pb isotope ratios can be explained as due to two end-member mixing of crustal Palaeoproterozoic Pb and a highly radiogenic Pb component. The age of this Pb mixing event cannot be constrained, and it is not clear whether the two events indicated by Re-Os and Pb systematics coincide. Thus, despite the fact that the textures, S isotopes and geochemical characteristics observed at Red Bore do not show obvious evidence of metamorphism or intense deformation, the occurrence of cryptic secondary remobilisation can be revealed by Re-Os and Pb isotope systems.

Red Bore and DeGrussa: part of the same hydrothermal system?

A genetic relationship between the Red Bore mineralisation and the strata-bound VHMS deposit at DeGrussa has been previously suggested (Hawke et al. 2015b; Pirajno et al. 2016). This interpretation is supported by the close spatial association, by mineralogical and geochemical arguments, for example the abundance of chalcopyrite, the enrichment in Cu, Au, Ag. However, the elongate geometry, level of mineralisation/grade (massive chalcopyrite with up to ~30 wt% Cu and low concentrations of Pb and Zn), the abundant massive magnetite mineralisation and the direct association with mafic intrusive host (dolerite) at Red Bore strongly contrast with DeGrussa and other VHMS deposits known in the region, which are mostly hosted by terrigenous sedimentary rocks. Typically, VHMS mineralisation tends to form sulfide-rich lensoid bodies, largely strata-bound and with thicknesses in the order of tens of metres and typically low aspect ratios (depth-to-lateral extent ratio). Massive sulfide mineralisation is formed at, or close to, the water-sediment interface, and is underlain by silica-sulfide stockwork style mineralisation (Shanks III 2012; Ohmoto 1996). Typical VHMS deposits associated with mafic volcanism have high Cu/(Cu+Zn) with Cu rarely exceeding 5 – 6 wt%, even in Cu-rich deposits (Galley et al. 2007; Shanks III 2012; Lobanov et al. 2014). Au-bearing pyrite-chalcopyrite discordant “pipes” have been described at Mount Morgan and Reward deposits, Australia (Large 1992). The Reward deposit has been attributed to the class of VHMS deposits based on the presence of strata-bound massive Zn-Pb-Cu lenses, alteration styles and ore textures (Large 1992). Murphy and Meyer (1998) described Au-rich massive chalcopyrite mineralisation hosted in mafic and ultramafic rocks of the Logatchev hydrothermal field of the Mid-Atlantic ridge. In these deposits sulfate (anhydrite) is rare, whereas it is abundant in associated Zn-rich deposits, a feature that Murphy and Meyer (1998) attribute to limited sea water contribution in Cu-rich deposits. The depth of deposition of the Red Bore mineralisation in the context of a submarine hydrothermal system cannot be assessed with certainty, given the absence of pressure indicators. However, the absence of widespread alteration suggests that the ore bodies did not form within the wide alteration zone typically associated with VHMS deposits.

At DeGrussa, reported $\delta^{34}S$ of sulfides span the range +0.25 to +9.82 ‰ (Hawke et al. 2015a), overlapping with our results at Red Bore, but also extending towards higher values. This may be due to mixing of magmatic fluids with sea water at, or near, the surface. In sea floor hydrothermal systems, as magmatic fluids rise towards the surface, they will inevitably mix with sea water-derived fluids, so that the resulting sulfide deposits will carry the geochemical features of both components. In some VHMS systems where a magmatic input has been inferred, the upwards widening of ranges of $\delta^{34}S$ in present-day hydrothermal vents (Petersen et al. 2014) as well as the upwards increase of $\Delta^{33}S$ (-1.5 to +1.2) in Archaean VHMS (Jamieson et al. 2013) suggests that VHMS-forming fluids become progressively sea water-enriched as they rise towards the surface. Seawater sulfate contributions to ancient VHMS deposits and present-day systems are estimated to vary from 3 to > 40 % (de Ronde et al. 2014; Jamieson et al. 2013; Chen et al. 2015). For example, hydrothermal fluids emitted at Clark volcano, Kermadec arc, and responsible for sea bed sulfate-sulfide mineralisation (dominated by barite, anhydrite and gypsum, or silica-Fe, with minor pyrite, sphalerite and galena), have been interpreted to be a mix of 40 % sea water with K-rich lava-derived magmatic fluids (de Ronde et al. 2014). Bell (2016) has measured S isotopes of various sulfides at DeGrussa using SIMS, and found that texturally primary pyrite, pyrrhotite and chalcopyrite have relatively low $\delta^{34}S$ (mostly +1 – +7 ‰), whereas overprinting euhedral pyrite has $\delta^{34}S$ of +8.4 – +29.1 ‰. This raises the possibility of contamination of bulk analyses by secondary pyrite.

Significance of magnetite mineralisation and magnetite breccia

Massive magnetite mineralisation is not present in all VHMS deposits, although VHMS systems in volcano-sedimentary successions where the volcanic component is predominantly mafic (Besshi and Cyprus types) are associated with banded iron formation (Galley et al. 2007; Sebert et al. 2004; Lydon 1984; Hannington 2014). These distal chemical precipitates (exhalites) are believed to form by precipitation from sea floor hydrothermal plumes during the early stages of hydrothermal activity

(Peter and Goodfellow 2003; Peter et al. 2007). In these deposits, magnetite is found together with finely layered quartz, magnetite, chlorite, Fe-carbonate, calcite and trace sulfides. Magnetite in these exhalites typically has high Mn (10^3 – 10^6 times sea water composition) and low Ti content (Peter and Goodfellow 2003; Dare et al. 2014). Magnetite is present in the Besshi-type Windy Craggy VHMS deposit of Canada, and intergrown magnetite and sulfide mineralisation has been described in the metamorphosed Cu-rich VHMS Fyre Lake deposit, Canada, and the Rudny-Altai, Russia, VHMS deposit (Sebert et al. 2004; Lobanov et al. 2014). Massive magnetite truncated by massive sulfide deposition has been described in Neoarchaean Cu-Zn VHMS deposits at Gossan Hill, Western Australia (Sharpe and Gemmell 2002). These authors interpreted this magnetite to have been deposited in the sub-surface, by sea water-derived hydrothermal fluids at T > 300°C, low-fS_2 low-fO_2, and reducing conditions, and the occurrence of carbonate in this massive magnetite suggests the presence of CO_2 in the fluids. The spatially-restricted magnetite halo around the massive chalcopyrite, as well as an abundance of carbonate veins in magnetite overprinted by later brecciation, suggest that Red Bore mineralisation is likely to have formed in a similar scenario.

Brecciation of magnetite in the Red Bore ore may have been caused by sudden release of overpressured fluids, similarly to what is observed in hydrothermal systems associated with intrusions (hydrothermal breccia). This mechanism has been proposed for breccia intersected by drilling in hydrothermal sea floor systems in the Manus basin (Binns et al. 2007). Fluid release during short-lived events of magma instability associated with volcanic activity has also been proposed (e.g. Christopher et al. 2010). Alternatively, brecciation may be caused by other processes, such as tectonic movements along faults. Fault movements and fluid release would have likely been closely related in a volcanically and tectonically active setting (Richards 2013), such as the one believed to be responsible for the formation of the Narracoota Formation, so that distinguishing between different mechanisms may not be possible.

A mineralisation model for Red Bore and comparison with modern sea floor hydrothermal systems

The direct observation of modern submarine hydrothermal vents represents a unique way of testing genetic mechanisms for VHMS systems formed in the geological past. Drilling through one of these systems hosted in turbiditic sediments in the Juan de Fuca spreading centre has revealed the presence of a deep (200 – 210 m below sea bed), Cu-rich massive sulfide zone with 50 vol% sulfides and 8 – 16 wt% Cu that impregnated relatively coarse-grained clastic sediments (Zierenberg et al. 1998). This zone, termed deep copper zone (DCZ) extends horizontally underneath an impermeable silicified horizon, in contrast to the vertical vein-rich zone that directly underlies the deposits on the surface (as described by Ohmoto 1996). These authors interpreted the DCZ as the lower part of a "feeder zone" to the hydrothermal system. Hardardóttir et al. (2009) have measured the composition of deep fluids in hydrothermal wells in Iceland, that were sampled at a depth of 1.3 – 1.5 km and temperature of 284 – 295°C. These authors found high concentrations of metals (Fe 9 – 140 ppm, Zn 79 – 393 ppm, Cu 207 – 261 ppm, Pb 120 – 290 ppm), orders of magnitude higher than black smoker fluids, and interpreted this compositional difference as indicating substantial metal deposition at depth in this type of environments. These data may imply that an underappreciated deep metal deposition takes place in association with VHMS deposits.

These observations lead us to interpret the Red Bore mineralised pipes as being the result of sub-surface deposition during strongly focussed fluid flow, possibly along structural discontinuities. In our preferred model, the mineralisation represents the escape pathway for magmatic-hydrothermal fluids released by a mafic intrusion. As an alternative, leaching of volcanic rocks may also explain the narrow $\delta^{34}S$ and high Se, admitting low sulfate contribution from S-poor sea water in Palaeoproterozoic times. However, a model implying magmatic-derived fluids seems to better fit different pieces of evidence. The first stage of mineralisation included the deposition of massive magnetite along the fluid conduit by low-fS_2 fluids, with subsequent brecciation due to tectonic or

446 hydrothermal processes. The trace element composition of magnetite at Red Bore falls in the "BIF"
447 field of the Al+Mn vs. Ti+V plot (Fig. 7) and is akin to chemical precipitates that form banded iron
448 formation in distal areas from submarine hydrothermal vents. Thus, fluids similar to the early Fe-rich
449 S-poor fluids at Red Bore may have been responsible for deposition of banded iron formation, which
450 is locally found in the Bryah Basin and are thought to be associated with sea floor hydrothermal
451 systems (Peter and Goodfellow 2003). Massive chalcopyrite was subsequently deposited by S-Cu-Fe-
452 rich fluids that exploited the same pathway. The anomalously high Cu concentrations at the centre
453 of the mineralisation are compatible with deposition from a S-Cu-Fe-rich magmatic volatile phase
454 similar to what described in mafic magma systems (Lowenstern et al. 1991; Yang and Scott 1996;
455 Simon and Ripley 2011). Narrow ranges of S isotopic compositions ($\delta^{34}S$ ~ 0 to +4 ‰), the presence
456 of Bi-Te-Se-(Ag-Au) phases and the low concentrations of Zn and Pb in comparison with typical
457 VHMS deposits are also compatible with a magmatic derivation of ore fluids with minor or no
458 interaction with sea water (Fig. 10). Eventually, these fluids may have ascended towards the surface
459 and contributed to the VHMS mineralisation known in the area (DeGrussa or similar VHMS deposits),
460 which has lower Cu contents and has $\delta^{34}S$ extending towards higher values.

461 The Cu-Au association is typical of footwall mineralisation deposited from high temperature
462 (300–350°C) fluids or mineralisation at mid-oceanic ridges (Murphy and Meyer 1998; Galley et al.
463 2007). In these high-temperature fluids, Au is mostly interpreted to be transported as Cl complexes
464 (Huston and Large 1989). However, others attribute Cu-Au mineralisation in sea floor mineralisation
465 to the high-temperature oxidation of $Au(HS)_2^-$ (Hannington et al. 1995).

466 In contrast to other sub-surface VHMS deposits where ore deposition occurred in stockwork-
467 style veins and pores of permeable rocks (e.g. volcaniclastic rocks at Hercules South, Tasmania; Khin
468 Zaw and Large 1992), the absence of open space-filling textures in our samples suggests that this
469 type of depositional mechanism was not predominant at Red Bore. Instead, ore deposition at Red

Bore occurred primarily by replacement, as shown by microtextures indicating sulfidation of precursor minerals (Fig. 3). Another prominent difference between Red Bore mineralisation and Hercules South is the low Cu contents (<1 wt%) of the latter, which is compatible with the low fluid temperatures estimated from fluid inclusion homogenisation temperatures (Khin Zaw and Large 1992).

Conclusions

The recent find at Red Bore prospect, Western Australia, includes elongate mineralisation several metres wide that has a zoned distribution of minerals: massive chalcopyrite at core (with Cu concentrations up to ~30 wt%) and brecciated massive magnetite at the margin. Mineralisation is hosted in Palaeoproterozoic mafic igneous rocks (mostly dolerite) and surrounded by a narrow talc-silica-carbonate alteration halo. In addition, disseminated sulfides intersected in proximity (hundreds of m) to the massive mineralisation is hosted by finely laminated mudrock. The mineralisation at Red Bore occurs in proximity to VHMS hosted sediments and mafic lavas at DeGrussa and the Cu-Ag-Au-rich composition of both deposits further supports a genetic relationship. However, the geometry of the mineralisation at Red Bore, the occurrence in shallow intrusive mafic rocks, as well as its mineralogical and trace element characteristics, set this mineralisation apart from associated VHMS deposits in the region and other VHMS systems worldwide. The mineralisation contains Ag and Au at hundreds and tens of ppm levels, respectively, and Bi, Te and Se at concentrations up to 100 – 1000 ppm. Gold is hosted in chalcopyrite, pyrite and in Bi-Te-(Se) phases, and no native Au was found. In situ S isotope analyses of pyrite and chalcopyrite indicate a narrow range of $\delta^{34}S$ (mostly +3.0 to +4.6 ‰), and $\Delta^{33}S \sim 0$. We interpret these mineralised bodies as having formed along strongly focussed pathways of fluid discharge, such as faults, along which S-rich fluids carried significant amounts of Cu, Fe, Au, Ag, Bi, Te and Se upwards towards the surface. Metals may have been derived from a degassing magma or from leaching of volcanic rocks. These fluids may have contributed to the

overlying VHMS systems. Analyses of both Re-Os isotopes and Pb isotopes of sulfides at Red Bore indicate open-system behaviour, and support mixing of crustal Pb with highly radiogenic Pb.

Acknowledgment

SIEF Science and Innovation Endowment Fund is acknowledged for funding this work. B. McDonald is thanked for assistance with LA-ICP-MS analysis. The authors would like to acknowledge the Australian Microscopy & Microanalysis Research Facility, AuScope, the Science and Industry Endowment Fund, and the State Government of Western Australian for contributing to the Ion Probe Facility at the Centre for Microscopy, Characterisation and Analysis at the University of Western Australia. This paper has benefited from reviews of D. Huston, Khin Zaw and G. Beaudoin.

504 **References**

505 Adamides NG (2010) Mafic-dominated volcanogenic sulphide deposits in the Troodos ophiolite,
506 Cyprus Part 2 – A review of genetic models and guides for exploration. Applied Earth Sci
507 119:193-204.

508 Agangi A, Reddy SM (2016) Open-system behaviour of magmatic fluid phase and transport of copper
509 in arc magmas at Krakatau and Batur volcanoes, Indonesia. J Volcanol Geothermal Res
510 327:669-686.

511 Bekker A, Barley ME, Fiorentini ML, Rouxel OJ, Rumble D, Beresford SW (2009) Atmospheric sulfur in
512 Archean komatiite-hosted nickel deposits. Science 326:1086-1089.

513 Bell JM (2016) In situ multiple sulphur isotope analysis of the DeGrussa VHMS deposit: Implications
514 for exploration and mineralisation. Honours thesis, University of Western Australia, 56 p.

515 Belousov I, Large RR, Meffre S, Danyushevsky LV, Steadman J, Beardsmore T (2016) Pyrite
516 compositions from VHMS and orogenic Au deposits in the Yilgarn Craton, Western Australia:
517 Implications for gold and copper exploration. Ore Geol Rev 79:474-499.

518 Berkenbosch HA, de Ronde CEJ, Gemmell JB, McNeill AW, Goemann K (2012) Mineralogy and
519 formation of black smoker chimneys from Brothers submarine volcano, Kermadec Arc. Econ
520 Geol 107:1613-1633.

521 Binns RA, Barriga FJAS, Miller DJ (2007) Leg 193 synthesis: anatomy of an active felsic-hosted
522 hydrothermal system, eastern Manus Basin, Papua New Guinea In: Barriga FJAS, Binns RA,
523 Miller DJ, Herzig PM (eds) Proc ODP, Sci Results, 193: College Station, TX (Ocean Drilling
524 Program). pp 1-71.

525 Chen M, Campbell IH, Xue Y, Tian W, Ireland TR, Holden P, Cas RAF, Hayman PC, Das R (2015)
526 Multiple sulfur isotope analyses support a magmatic model for the volcanogenic massive
527 sulfide deposits of the Teutonic Bore Volcanic Complex, Yilgarn Craton, Western Australia.
528 Econ Geol 110:1411-1423.

529 Christopher T, Edmonds M, Humphreys MCS, Herd RA (2010) Volcanic gas emissions from Soufrière
530 Hills Volcano, Montserrat 1995-2009, with implications for mafic magma supply and
531 degassing. Geophys Res Lett 37. doi: 10.1029/2009GL041325.
532 Ciobanu C, Cook NJ, Pring A (2005) Bismuth tellurides as gold scavengers Mineral deposit research:
533 Meeting the global challenge. Springer Berlin Heidelberg, pp 1383-1386.
534 Ciobanu CL, Cook NJ, Damian F, Damian G (2006) Gold scavenged by bismuth melts: An example
535 from Alpine shear-remobilizates in the Highiş Massif, Romania. Mineral Petrol 87:351-384.
536 Cloutier J, Piercey SJ, Layne G, Heslop J, Hussey A, Piercey G (2015) Styles, textural evolution,
537 and sulfur isotope systematics of Cu-rich sulfides from the Cambrian Whalesback
538 volcanogenic massive sulfide deposit, central Newfoundland, Canada. Econ Geol 110:1215-
539 1234.
540 Dare SAS, Barnes S-J, Beaudoin G, Méric J, Boutroy E, Potvin-Doucet C (2014) Trace elements in
541 magnetite as petrogenetic indicators. Miner Deposita 49:785-796.
542 de Ronde CEJ, Hannington MD, Stoffers P, Wright IC, Ditchburn RG, Reyes AG, Baker ET, Massoth GJ,
543 Lupton JE, Walker SL, Greene RR, Soong CWR, Ishibashi J, Lebon GT, Bray CJ, Resing JA (2005)
544 Evolution of a submarine magmatic-hydrothermal system: Brothers volcano, southern
545 Kermadec Arc, New Zealand. Econ Geol 100:1097-1133.
546 de Ronde CEJ, Walker SL, Ditchburn RG, Tontini FC, Hannington MD, Merle SG, Timm C, Handler MR,
547 Wysoczanski RJ, Dekov VM, Kamenov GD, Baker ET, Embley RW, Lupton JE, Stoffers P (2014)
548 The anatomy of a buried submarine hydrothermal system, Clark Volcano, Kermadec Arc,
549 New Zealand. Econ Geol 109:2261-2292.
550 Dora ML, Singh H, Kundu A, Shareef M, Randive KR, Joshi S (2014) Tsumoite (BiTe) and associated Ni-
551 PGE mineralization from Gondpipri mafic-ultramafic complex, Bastar Craton, Central India:
552 mineralogy and genetic significance. Centr Eur J Geol 4: 506-517.

553 Drummond SE, Ohmoto H (1985) Chemical evolution and mineral deposition in boiling hydrothermal
554 systems. Econ Geol 80:126-147.
555 Dupuis C, Beaudoin G (2011) Discriminant diagrams for iron oxide trace element fingerprinting of
556 mineral deposit types. Miner Deposita 46:319-335.
557 Farquhar J, Wu N, Canfield DE, Oduro H (2011) Connections between sulfur cycle evolution, sulfur
558 isotopes, sediments, and base metal sulfide Deposits. Econ Geol 105:509-533.
559 Galley AG (2003) Composite synvolcanic intrusions associated with Precambrian VMS-related
560 hydrothermal systems. Miner Deposita 38:443-473.
561 Galley AG, Hannington M, Jonasson IR (2007) Volcanogenic massive sulphide deposits In: Goodfellow
562 WD (ed) Mineral deposits of Canada: A synthesis of major deposit-types, district
563 metallogeny, the evolution of geological provinces, and exploration methods. Geol Assoc
564 Canada, Mineral Deposits Division, pp 141-161.
565 Gemmell JB, Sharpe R, Jonasson IR, Herzig PM (2004) Sulfur isotope evidence for magmatic
566 contributions to submarine and subaerial gold mineralization: Conical seamount and the
567 Ladolam gold deposit, Papua New Guinea. Econ Geol 99:1711-1725.
568 Hannington MD (2014) 13.18 - Volcanogenic massive sulfide deposits In: Turekian HDHK (ed)
569 Treatise on Geochemistry (Second Edition). Elsevier, Oxford, pp 463-488.
570 Hannington M, Herzig P, Scott S, Thompson G, Rona P (1991) Comparative mineralogy and
571 geochemistry of gold-bearing sulfide deposits on the mid-ocean ridges. Marine Geol
572 101:217-248.
573 Hardardóttir V, Brown KL, Fridriksson T, Hedenquist JW, Hannington MD, Thorhallsson S (2009)
574 Metals in deep liquid of the Reykjanes geothermal system, southwest Iceland: Implications
575 for the composition of seafloor black smoker fluids. Geology 37:1103-1106.

576 Hawke ML, Davidson GJ, Meffre S, Hilliard P, Large R, Gemmell JB (2015a) Geological Evolution of the
577 DeGrussa Cu-Au-Ag Volcanic-Hosted Massive Sulfide Deposit, Western Australia. SEG 2015
578 conference. Hobart, Australia, Poster.
579 Hawke ML, Meffre S, Stein H, Hilliard P, Large R, Gemmell JB (2015b) Geochronology of the DeGrussa
580 volcanic-hosted massive sulphide deposit and associated mineralisation of the Yerrida, Bryah
581 and Padbury Basins, Western Australia. Precamb Res 267:250-284.
582 Heinrich CA, Ryan CG, Mernagh TP, Eadington PJ (1992) Segregation of ore metals between
583 magmatic brine and vapor: a fluid inclusion study using PIXE microanalysis. Econ Geol
584 87:1566-1583.
585 Henley RW, Mavrogenes J, Tanner D (2012) Sulfosalt melts and heavy metal (As-Sb-Bi-Sn-Pb-Tl)
586 fractionation during volcanic gas expansion: the El Indio (Chile) paleo-fumarole. Geofluids
587 12:199-215.
588 Huston D, Relvas JRS, Gemmell JB, Drieberg S (2011) The role of granites in volcanic-hosted massive
589 sulphide ore-forming systems: an assessment of magmatic–hydrothermal contributions.
590 Miner Deposita 46:473-507.
591 Huston DL, Pehrsson S, Eglington BM, Khin Zaw (2010) The geology and metallogeny of volcanic-
592 hosted massive sulfide deposits: variations through geologic time and with tectonic setting.
593 Econ Geol 105:571-591.
594 Huston DL, Large RR (1989) A chemical model for the concentration of gold in volcanogenic massive
595 sulfide deposits. Ore Geol Rev 4: 171-200.
596 Hynes A, Gee RD (1986) Geological setting and petrochemistry of the Narracoota Volcanics,
597 Capricorn Orogen, Western Australia. Precamb Res 31:107-132.
598 Jamieson JW, Wing BA, Farquhar J, Hannington MD (2013) Neoarchaean seawater sulphate
599 concentrations from sulphur isotopes in massive sulphide ore. Nature Geosci 6:61-64.

600 Kajiwara Y, Krouse HR (1971) Sulfur isotope partitioning in metallic sulfide systems. Can J Earth Sci
601 8:1397-1408.
602 Kamenetsky VS, Binns RA, Gemmell JB, Crawford AJ, Mernagh TP, Maas R, Steele D (2001) Parental
603 basaltic melts and fluids in eastern Manus backarc Basin: Implications for hydrothermal
604 mineralisation. Earth Planet Sci Lett 184:685-702.
605 Keith M, Häckel F, Haase KM, Schwarz-Schampera U, Klemd R (2016) Trace element systematics of
606 pyrite from submarine hydrothermal vents. Ore Geol Rev 72, Part 1:728-745.
607 Khin Zaw, Large RR (1992) The precious metal-rich, South Hercules mineralization, western
608 Tasmania; a possible subsea-floor replacement volcanic-hosted massive sulfide deposit.
609 Econ Geol 87:931-952.
610 Large R, Doyle M, Raymond O, Cooke D, Jones A, Heasman L (1996) Evaluation of the role of
611 Cambrian granites in the genesis of world class VHMS deposits in Tasmania. Ore Geol Rev
612 10:215-230.
613 Large RR (1992) Australian volcanic-hosted massive sulfide deposits; features, styles, and genetic
614 models. Econ Geol 87:471-510.
615 Layton-Matthews D, Peter JM, Scott SD, Leybourne MI (2008) Distribution, mineralogy, and
616 geochemistry of selenium in felsic volcanic-hosted massive sulfide deposits of the Finlayson
617 Lake District, Yukon Territory, Canada. Econ Geol 103:61-88.
618 Lehmann, B. Zhao, X., Zhou, M., Du, A., Mao, J., Zeng, P., Henjes-Kunst, F., Heppe, K., 2013. Mid-
619 Silurian back-arc spreading at the northeastern margin of Gondwana: The Dapingzhang
620 dacite-hosted massive sulfide deposit, Lancangjiang zone, southwestern Yunnan, China.
621 Gondwana Research, 24: 648-663.
622 Lobanov K, Yakubchuk A, Creaser RA (2014) Besshi-type VMS deposits of the Rudny Altai (Central
623 Asia). Econ Geol 109:1403-1430.

624 Lowenstern JB, Mahood GA, Rivers ML, Sutton SR (1991) Evidence for extreme partitioning of copper
625 into a magmatic vapor-phase. Science 252:1405-1409.
626 Lydon JW (1984) Ore deposit models - 8. Volcanogenic massive suphide deposits. Part I: A
627 descriptive model. Geosci Canada 11:195-202.
628 Marcoux E, Moëlo Y, Leistel JM (1996) Bismuth and cobalt minerals as indicators of stringer zones to
629 massive sulphide deposits, Iberian Pyrite Belt. Miner Deposita 31:1-26.
630 Marini L, Moretti R, Accornero M (2011) Sulfur isotopes in magmatic-hydrothermal systems, melts,
631 and magmas. Rev Mineral Geochem 73:423-492.
632 Maslennikov VV, Maslennikova SP, Large RR, Danyushevsky LV, Herrington RJ, Stanley CJ (2013)
633 Tellurium-bearing minerals in zoned sulfide chimneys from Cu-Zn massive sulfide deposits of
634 the Urals, Russia. Mineral Petrol 107:67-99.
635 Moss R, Scott SD, Binns RA (2001) Gold content of eastern Manus Basin volcanic rocks: implications
636 for enrichment in associated hydrothermal precipitates. Econ Geol 96:91-107.
637 Murphy PJ, Meyer G (1998) A gold-copper association in ultramafic-hosted hydrothermal sulfides
638 from the Mid-Atlantic Ridge. Econ Geol 93:1076-1083.
639 Nadoll P, Angerer T, Mauk JL, French D, Walshe J (2014) The chemistry of hydrothermal magnetite: A
640 review. Ore Geol Rev 61:1-32.
641 Occhipinti SA, Sheppard S, Nelson DR, Myers JS, Tyler IM (1998a) Syntectonic granite in the southern
642 margin of the Palaeoproterozoic Capricorn Orogen, Western Australia. Austr J Earth Sci
643 45:509-512.
644 Occhipinti SA, Swager CP, Pirajno F (1998b) Structural-metamorphic evolution of the
645 Palaeoproterozoic Bryah and Padbury Groups during the Capricorn orogeny, Western
646 Australia. Precamb Res 90:141-158.

647 Occhipinti SA, Sheppard S, Passchier C, Tyler IM, Nelson DR (2004) Palaeoproterozoic crustal
648 accretion and collision in the southern Capricorn Orogen: the Glenburgh Orogeny. Precamb
649 Res 128:237-255.
650 Ohmoto H (1986) Stable isotope geochemistry of ore deposits. Rev Mineral Geochem 16:491-559.
651 Ohmoto H (1996) Formation of volcanogenic massive sulfide deposits: The Kuroko perspective. Ore
652 Geol Rev 10:135-177.
653 Peter JM, Goodfellow WD (2003) Hydrothermal sedimentary rocks of the Heath Steele Belt, Bathurst
654 Mining Camp, New Brunswick. 3. Application of hydrothermal sediment mineralogy and
655 mineral and bulk composition to the exploration for concealed massive sulfide
656 mineralization In: Goodfellow WD, McCutcheon SR, Peter JM (eds) Massive sulphide
657 deposits of the Bathurst mining camp, New Brunswick, and Northern Maine. Economic
658 Geology, Monograph 11 pp 417-433.
659 Peter JM, Layton-Matthews D, Piercey S, Bradshaw G, Paradis S, Boulton A (2007) Volcanic-hosted
660 massive sulphide deposits of the Finlayson Lake District, Yukon In: Goodfellow WD (ed)
661 Mineral deposits of Canada: A synthesis of major deposit-types, district metallogeny, the
662 evolution of geological provinces, and exploration methods. Geol Assoc Canada, Mineral
663 Deposits Division, pp 471-508.
664 Petersen S, Monecke T, Westhues A, Hannington MD, Gemmell JB, Sharpe R, Peters M, Strauss H,
665 Lackschewitz K, Augustin N, Gibson H, Kleeberg R (2014) Drilling shallow-water massive
666 sulfides at the Palinuro Volcanic Complex, Aeolian Island Arc, Italy. Econ Geol 109:2129-
667 2158.
668 Pirajno F, Occhipinti SA (2000) Three Palaeoproterozoic basins-Yerrida, Bryah and Padbury-Capricorn
669 Orogen, Western Australia. Austral J Earth Sci 47:675-688.

670 Pirajno F, Occhipinti SA, Swager CP (2000) Geology and mineralisation of the Palaeoproterozoic
671 Bryah and Padbury basins Western Australia. Geol Surv Western Australia, Dept Minerals
672 Energy, 52 p.
673 Pirajno F, Jones JA, Hocking RM, Halilovic J (2004) Geology and tectonic evolution of
674 Palaeoproterozoic basins of the eastern Capricorn Orogen, Western Australia. Precamb Res
675 128:315-342.
676 Pirajno F, Chen Y, Li N, Li C, Zhou L-m (2016) Besshi-type mineral systems in the Palaeoproterozoic
677 Bryah Rift-Basin, Capricorn Orogen, Western Australia: Implications for tectonic setting and
678 geodynamic evolution. Geosci Frontiers 7:345-357.
679 Reddy SM, Occhipinti SA (2004) High-strain zone deformation in the southern Capricorn Orogen,
680 Western Australia: kinematics and age constraints. Precamb Res 128:295-314.
681 Richards JP (2013) Giant ore deposits formed by optimal alignments and combinations of geological
682 processes. Nature Geosci 6:911-916.
683 Ripley EM, Li C (2003) Sulfur isotope exchange and metal enrichment in the formation of magmatic
684 Cu-Ni-(PGE) deposits. Econ Geol 98:635-641.
685 Ross P-S, Mercier-Langevin P (2014) Igneous rock associations 14. The volcanic setting of VMS and
686 SMS deposits: A review. GeosciCanada 41 (3).
687 Sandfire Resources Report (2016) DeGrussa mine plan, mineral resource and ore reserve update.
688 www.sandfire.com.au.
689 Sebert C, Hunt J, Foreman IJ (2004) Geology and lithogeochemistry of the Fyre Lake copper-cobalt-
690 gold sulphide-magnetite deposit, southeastern Yukon Yukon Geological Survey Open file
691 2004-17. pp 46.
692 Shanks III WC (2001) Stable isotopes in seafloor hydrothermal systems: vent fluids, hydrothermal
693 deposits, hydrothermal alteration, and microbial processes. Rev Mineral Geochem 43:469-
694 525.

695 Shanks III WC (2012) Hydrothermal alteration in volcanogenic massive sulfide occurrence model. US
696 Geol Surv Sci Invest Report 2010–5070 –C. 12 p.
697 Sharpe R, Gemmell JB (2002) The Archean Cu-Zn magnetite-rich Gossan Hill volcanic-hosted massive
698 sulfide deposit, Western Australia: Genesis of a multistage hydrothermal system. Econ Geol
699 97:517-539.
700 Simon AC, Ripley EM (2011) The role of magmatic sulfur in the formation of ore deposits. Rev
701 Mineral Geochem 73:513-578.
702 Solomon M, Gemmell JB, Khin Zaw (2004) Nature and origin of the fluids responsible for forming the
703 Hellyer Zn–Pb–Cu, volcanic-hosted massive sulphide deposit, Tasmania, using fluid
704 inclusions, and stable and radiogenic isotopes. Ore Geol Rev 25:89-124.
705 Stacey JS, Kramers JD (1975) Approximation of terrestrial lead isotopic evolution by a two-stage
706 model. Earth Planet Sci Letts 26:207-221.
707 Sun W, Arculus RJ, Kamenetsky VS, Binns RA (2004) Release of gold-bearing fluids in convergent
708 margin magmas prompted by magnetite crystallization. Nature 431:975-978.
709 Symonds RB, Rose WI, Reed MH, Lichte FE, Finnegan DL (1987) Volatilization, transport and
710 sublimation of metallic and non-metallic elements in high temperature gases at Merapi
711 Volcano, Indonesia. Geochim Cosmochim Acta 51:2083-2101.
712 Timm C, de Ronde CEJ, Leybourne MI, Layton-Matthews D, Graham IJ (2012) Sources of chalcophile
713 and siderophile elements in Kermadec Arc lavas. Econ Geol 107:1527-1538.
714 Urabe T, Marumo K (1991) A new model for Kuroko-type deposits of Japan. Episodes 14:246–251.
715 Wohlgemuth-Ueberwasser CC, Viljoen F, Petersen S, Vorster C (2015) Distribution and solubility
716 limits of trace elements in hydrothermal black smoker sulfides: An in-situ LA-ICP-MS study.
717 Geochim Cosmochim Acta 159:16-41.
718 Yang K, Scott SD (1996) Possible contribution of a metal-rich magmatic fluid to a sea-floor
719 hydrothermal system. Nature 383:420-423.

720 Yeats CJ, Parr JM, Binns RA, Gemmell JB, Scott SD (2014) The SuSu Knolls hydrothermal field, eastern
721 Manus basin, Papua New Guinea: An active submarine high-sulfidation copper-gold system.
722 Econ Geol 109:2207-2226.
723 Zierenberg RA, Fouquet Y, Miller DJ, Bahr JM, Baker PA, Bjerkgard T, Brunner CA, Duckworth RC,
724 Gable R, Gieskes J, Goodfellow WD, Groschel-Becker HM, Guerin G, Ishibashi J, Iturrino G,
725 James RH, Lackschewitz KS, Marquez LL, Nehlig P, Peter JM, Rigsby CA, Schultheiss P, Shanks
726 WC, Simoneit BRT, Summit M, Teagle DAH, Urbat M, Zuffa GG (1998) The deep structure of a
727 sea-floor hydrothermal deposit. Nature 392:485-488.
728

729 **Figure captions**

730 **Fig. 1 A** Simplified geological map of the Bryah, Padbury, and Yerrida Basins and distribution of
731 VHMS and other ore deposits. Inset: location of the Capricorn Orogen in Western Australia between
732 the Pilbara and Yilgarn cratons is indicated in grey shade. Modified from Pirajno et al. (1998, 2000);
733 sulfide Re-Os ages from Hawke et al. (2015b). **B** Map of magnetic anomalies of the Red Bore area
734 with location of some drill holes. Airborne magnetic survey included 1799 km flown at sensor height
735 of 30 m using a Radiation Solutions RD-500 spectrometer (more information on the magnetic survey
736 available in the 09/02/2015 Report at www.thundelarra.com/news/). **C** Down-hole plots of Cu
737 assays. **D** Simplified logs of two cores (TRBDD06 and TRBDD08)

738 **Fig. 2** Drill core samples from Red Bore. **A** Massive chalcopyrite, sample TRCDD09 32.0 m. **B** Massive
739 magnetite breccia. Clasts are cross-cut by Fe-Ca-carbonate (cb) veinlets that do not extend into the
740 matrix. **C** External contact of the ore body. Chalcopyrite veinlets (Ccp, some arrowed) truncate
741 magnetite (Mag) at the contact with talc-silica-carbonate-amphibole altered host rock (sil)

742 **Fig. 3** Ore microtextures at Red Bore. **A** (and inset) Massive chalcopyrite with needle-like silicate
743 inclusions. BSE image, sample TRBDD09 35.5m. **B** Anhedral pyrite and partially sulfidised silicate
744 needles (some arrowed) in chalcopyrite. Note the “cleaved” texture of pyrite. BSE image, sample
745 TRCDD09 31.5 m. **C** Massive magnetite with chalcopyrite veinlets. BSE image, sample TRCDD04 31.5
746 m. **D** Fe-carbonate-amphibole veinlet with minor sulfides (chalcopyrite, sphalerite, Co-sulfide) cross-
747 cutting massive magnetite. BSE image, sample TRBDD09 38 m. **E** Inclusion of Bi-Te and Ag-Te in
748 pyrite. BSE image, sample TRCDD04 31.5 m. **F** BSE image and X-ray element maps of zoned S-Co-O-Si
749 mixed phase in strongly silicified needle-like crystals (BSE, sample TRBDD09 35.5 m). Note S-
750 replacement along rim and cracks (sulfidation of silicates). Abbreviations: Am amphibole, cb
751 carbonate, Ccp chalcopyrite, Mag magnetite, Py pyrite, Sp sphalerite, sil silicates (variably silicified
752 talc and amphibole)

753 **Fig. 4** Bulk rock assays of Red Bore samples (ICP-OES and ICP-MS). Au and Ag as ppm, Cu as wt%

754 **Fig. 5** Trace element composition of chalcopyrite and pyrite from Red Bore (LA-ICP-MS, all
755 compositions as ppm). Samples from the centre (massive chalcopyrite) and the margin (massive
756 magnetite) of the mineralised body are distinguished

757 **Fig. 6** Laser ablation signal as counts per second (cps) of chalcopyrite (**A**) and pyrite (**B**) plotted
758 versus analysis time (s). Co-occurrence of element peaks indicates the presence of Te-Au-Ag and Bi-
759 Te inclusions. **A** total Au = 7.7 ppm, sample TRBDD08 51.7 m; **B** total Au = 0.02 ppm, sample
760 TRCDD09 31.5 m

761 **Fig. 7** Trace element compositions of magnetite at Red Bore (LA-ICP-MS). **A** Ti vs Ni/Cr diagram; line
762 distinguishing magmatic and hydrothermal magnetite and fields from Dare et al. (2014). **B** Al + Mn
763 vs. Ti + Mn (wt%) diagram from Dupuis and Beaudoin (2011), BIF field modified according to Nadoll
764 et al. (2014)

765 **Fig. 8** Sulfur isotope compositions at Red Bore (SIMS). **A** histogram, **B** plots of single analyses
766 distinguished by sample and mineral phase. Abbreviations: Ccp chalcopyrite, Py pyrite. Ranges of
767 $\delta^{34}S$ for VHMS deposits (DeGrussa; Hawke et al. 2015a; Bell 2016; other data compiled by Lobanov et
768 al. 2014) and S-poor mafic complexes are shown for comparison; Bushveld and Stillwater complexes
769 (from Ripley and Li 2003)

770 **Fig. 9** Composition of pyrite and chalcopyrite from Red Bore (LA-ICP-MS, all compositions as ppm),
771 including disseminated mineralisation compared with pyrite from modern submarine vents formed
772 in a comparable spreading setting (Wohlgemuth-Ueberwasser et al. 2015; Keith et al. 2016)

773 **Fig. 10** A possible genetic model for the formation of Red Bore mineralised pipes and co-genetic
774 VHMS deposits at DeGrussa. In this model, Cu, Au, Ag, Bi and other metals were transported from a
775 magmatic fluid phase and fed into VHMS deposits at the surface, where they would have mixed with

776 sea water-derived fluids. Other elements, such as Zn, are found in VHMS deposits but are depleted
777 at Red Bore and may have been derived from leaching of the volcano-sedimentary succession by sea
778 water-derived hydrothermal fluids

779 **ESM Fig. 1** Plots of Pb isotope ratios (LA-ICP-MS) of chalcopyrite and pyrite from Red Bore compared
780 with values from the DeGrussa VHMS deposit (Hawke et al. 2015b; Belousov et al. 2016)

781 **ESM Fig. 2** Re-Os analyses of sulfides from Red Bore (6 out of 10 analyses are plotted)

782 **ESM Fig 3** Comparison of S isotope compositions of Red Bore and other VHMS deposits throughout
783 Earth's history. Compilation of VHMS by Huston et al. (2010), sea water sulfide and pyrite from
784 Farquhar et al. (2011), DeGrussa sulfide analyses from Hawke et al. (2015a)

785

ESM1 – Analytical conditions

Samples collected from drill core were prepared as polished bock mounts and thin sections and observed under optical and scanning electron microscope (SEM). SEM microtextural and mineralogical observations were made at the John de Laeter Centre at Curtin University using a Tescan Mira field emission scanning electron microscope (FE-SEM) equipped with back-scattered electron (BSE) and energy dispersion spectrometry (EDS) detectors. EDS was used to identify minerals. An acceleration of 20 kV and spot size <1 µm were used.

Bulk assays

A total of 474 assays of mineralised and weakly mineralised samples from 14 drill cores, were acquired by Thundelarra Ltd. as part of the exploration procedures on 1 m-long core intervals and obtained by ICP-OES and ICP-MS after four-acid digestion. Analyses were performed at Intertek Genalysis in Maddington, Western Australia (www.intertek.com). All analyses and further analytical details are available in Thundelarra Reports at www.thundelarra.com/news.

Laser ablation inductively-coupled plasma mass spectrometry (LA-ICP-MS)

Trace element compositions of sulfide phases and magnetite were investigated using a Coherent CompEX 193 nm laser and an Agilent 7700 quadrupole mass spectrometer at Curtin University. Ablation was performed at 7 Hz repetition rate, 75 µm spot size and approximately 2.5 J/cm^2 fluence. During the analyses, 20 s of background acquisition were followed by 30 s of ablation. The following masses have been monitored: ^{24}Mg, ^{27}Al, ^{28}Si, ^{34}S, ^{43}Ca, ^{49}Ti, ^{51}V, ^{53}Cr, ^{55}Mn, ^{57}Fe, ^{59}Co, ^{60}Ni, ^{65}Cu, ^{66}Zn, ^{75}As, ^{77}Se, ^{95}Mo, ^{108}Pd, ^{107}Ag, ^{111}Cd, ^{118}Sn, ^{121}Sb, ^{125}Te, ^{157}Gd, ^{185}Re, ^{195}Pt, ^{197}Au, ^{202}Hg, ^{205}Tl, ^{206}Pb, ^{207}Pb, ^{208}Pb and ^{209}Bi. Each mass was analysed for 0.02 – 0.03 s (total sweep approximate time 0.5 s). Quantification of element concentrations was obtained using glass NIST 610, sulfide BONN and sulfide PO726 (Jochum et al. 2011) as reference materials, whereas glasses NIST612 and

GSD-1g were used as secondary standards. Iron, inferred by stoichiometry, was used as the known element (internal standard) for pyrite, chalcopyrite and magnetite.

Secondary ion mass spectrometry (SIMS) multiple isotope S analyses

Sample mounts were made by coring 3 mm diameter pucks from rock fragments that were mounted and cast in an epoxy mount and polished with 1 µm polishing powder. Quadruple sulfur isotopes (^{32}S, ^{33}S, ^{34}S) were measured using a CAMECA SIMS1280 large-geometry ion microprobe at the Centre for Microscopy, Characterisation and Analysis at the University of Western Australia. Sample mounts were trimmed to a thickness of 5 mm, coated with 30 nm of gold, and fitted with a standard block co-inserted in the sample holder. All information regarding sample preparation, a standard block, analytical procedures, data reduction, and reference material are reported by LaFlamme et al. (2016). A 10 keV Cs^+ primary beam that operated at 2.2-2.6 nA in Gaussian mode bombarded the sample surface and a 20 µm raster was applied. Charge compensation was provided using a normal incidence electron flood gun. Following a pre-sputter (30 s with a raster size of 30 µm), secondary sulfur ions from the target sample were extracted at -10 kV and admitted to the mass spectrometer (field magnification of ×133), with automated centring of the secondary beam in the field aperture (both x and y; aperture size 4000 µm) and entrance slit (x direction only; slit width 60 µm). The NMR magnetic field controller locked the axial mass at the beginning of each session.

The mass spectrometer operated at a mass resolution (M/ΔM) of about 2500 (exit slit width of 500 µm on the multicollector), which provides a wider flat peak top than using 250 um exit slit (nominal mass resolution ca. 5000). The H1 detector collecting ^{33}S was moved slightly towards higher masses to keep away from the $^{32}S^1H$ peak. Isotopes ^{32}S, ^{33}S, and ^{34}S were detected by three Faraday Cups in the multicollector system with amplifiers with 1011 Ω (L'2) and 1010 Ω (L1 and H1) resistors. The measurement of ^{36}S utilised a low noise ion counting electron multiplier (EM) on H2 detector at high count rate (~300 kcps). The EM high voltage was optimised using a Pulse Height Amplitude

(PHA) Distribution Curve at the start of each session, and the grain drift was measured three times during each analysis and corrected by the CAMECA CIPS software. Acquisition time was 279 s in 45 integration cycles including the EM gain drift measurement time. Measurements of unknowns were interspersed with matrix-matched reference material (Sierra pyrite [$\delta^{33}S$ = 1.09± 0.02 ‰; $\delta^{34}S$ = 2.17 ± 0.04‰] and Nifty-b chalcopyrite [$\delta^{33}S$ = -1.78± 0.03 ‰; $\delta^{34}S$ = -3.58± 0.07 ‰]; LaFlamme et al. 2016) to calibrate isotope ratios, correct for drift, and monitor internal precision. Uncertainties on each $\delta^{x}S$ value were calculated by propagating the errors on instrumental mass fractionation determination, reference value of the matrix-matched standard and internal error on each sample raw data point. $\Delta^{33}S$ and values were calculated using the calibrated $\delta^{33}S$ and $\delta^{34}S$ values and theoretical equations of mass-dependant fractionation for sulfur isotopes.

Re-Os isotope analyses

Five samples of massive sulfide and disseminated sulfides in massive magnetite have been analysed for Re-Os. Each samples was analysed twice, for a total of ten analyses. The Re-Os analytical procedures we used have been fully described elsewhere (Nozaki et al. 2013; 2014). Powdered sulfide samples (<350 mm) were initially separated using CH_2I_2 heavy liquid to remove any silicate minerals. All Re-Os measurements were made with a negative thermal ionization mass spectrometer (NTIMS; ThermoFinnigan TRITON) at Japan Agency for Marine-Earth Science and Technology (JAMSTEC). Re and Os concentrations were determined by the isotope dilution method combined with Carius tube digestion (Shirey and Walker 1995), CCl_4 and HBr extraction of Os (Cohen and Waters 1996), Os purification by microdistillation (Roy-Barman and Allègre 1994), and Re separation by anion exchange chromatography (Morgan et al. 1991). Approximately 300 mg of separated sulfide sample was weighed, spiked with ^{185}Re and ^{190}Os, and digested in10 mL of inverse aqua regia in a sealed Carius tube at 220°C for 24 h. After cooling, the Carius tube was opened carefully, and the solution was transferred to a 30-mL PFA vessel into which 4 mL of CCl_4 was added. This mixture was shaken for 3 min and, after centrifugation, the CCl_4 was transferred to a20-mL PFA

vessel. The CCl_4 Os-extraction process was performed three times, after which 4 mL of HBr was added to the Os-bearing CCl_4 solution and subsequently warmed under a heat lamp for 1 h. After removal of the CCl_4 fraction, the Os bearing HBr fraction was gently evaporated and purified by microdistillation. Re was separated from the aqueous phase remaining after CCl_4 extraction of Os in a Muromac AG 1-X8 anion exchange resin.

Re and Os isotope compositions were measured in static multiple Faraday collector mode and pulse-counting electron multiplier mode, respectively. From the measured oxide ratios of ReO_4^- and OsO_3^-, atomic ratios of Re and Os were calculated after correction for oxide interference. Oxide corrections were made using $^{17}O/^{16}O = 0.00037$ and $^{18}O/^{16}O = 0.002045$ (Nier 1950). Instrumental mass fractionation of Os was corrected against a stable $^{192}Os/^{188}Os$ ratio of 3.08271. For precise analysis of Re isotope composition, a total evaporation method (Suzuki et al. 2004) was applied to eliminate the effect of instrumental mass fractionation during measurement. The total procedural blank was ~3.7 pg for Re and ~2.7 pg for Os with a $^{187}Os/^{188}Os$ ratio of ~0.14. The precision of the $^{187}Os/^{188}Os$ measurements, based on analysis of a Johnson Matthey Chemicals Os standard solution over a period of several months, was better than 0.4% (2σ). The Re-Os dates were determined by using Re-Os isotope data with the Isoplot v. 3 software.

References

LaFlamme C, Martin L, Jeon H, Reddy SM, Selvaraja V, Caruso S, Bui TH, Roberts MP, Voute F, Hagemann S, Wacey D, Littman S, Wing B, Fiorentini M, Kilburn MR (2016) In situ multiple sulfur isotope analysis by SIMS of pyrite, chalcopyrite, pyrrhotite, and pentlandite to refine magmatic ore genetic models. Chem Geol 444:1-15.

Jochum KP, Weis U, Stoll B, Kuzmin D, Yang Q, Raczek I, Jacob DE, Stracke A, Birbaum K, Frick DA, Günther D, Enzweiler J (2011) Determination of reference values for NIST SRM 610–617 glasses following ISO guidelines. Geostand Geoanalyt Res 35:397-429.

Nozaki T, Kato Y, Suzuki K (2013) Late Jurassic ocean anoxic event: evidence from voluminous sulphide deposition and preservation in the Panthalassa. Sci Reports 3:1889.

Nozaki T, Kato Y, Suzuki K (2014) Re-Os geochronology of the Hitachi volcanogenic massive sulfide deposit: The oldest ore deposit in Japan. Econ Geol 109:2023-2034.

Roy-Barman M, Allègre CJ (1994) $^{187}Os^{186}Os$ ratios of mid-ocean ridge basalts and abyssal peridotites. Geochim Cosmochim Acta 58:5043-5054.

Shirey SB, Walker RJ (1995) Carius tube digestion for low-blank rhenium-osmium analysis. Analyt Chem 67:2136-2141.

Morgan JW, Golightly DW, Dorrzapf Jr AF (1991) Methods for the separation of rhenium, osmium and molybdenum applicable to isotope geochemistry. Talanta 38:259-265.

Cohen AS, Waters FG (1996) Separation of osmium from geological materials by solvent extraction for analysis by thermal ionisation mass spectrometry. Analytica Chimica Acta 332:269-275.

Cook NJ, Ciobanu CL, Mao J (2009) Textural control on gold distribution in As-free pyrite from the Dongping, Huangtuliang and Hougou gold deposits, North China Craton (Hebei Province, China). Chem Geol 264:101-121.

Nier AO (1950) A redetermination of the relative abundances of the isotopes of carbon, nitrogen, oxygen, argon, and potassium. Physical Rev 77:789-793.

Suzuki K, Miyata Y, Kanazawa N (2004) Precise Re isotope ratio measurements by negative thermal ionization mass spectrometry (NTI-MS) using total evaporation technique. Internat J Mass Spectrom 235:97-101.

ESM2 Drill hole locations at Red Bore

Hole	East	North	RL	Depth	Dip	Azimuth	Data published online
TRBDD01	735920	7172551	577m	45.1m	-70°	222°	May-14
TRBDD02	735927	7172559	577m	60.3m	-75°	220°	May-14
TRBDD03	735918	7172548	577m	35.5m	-70°	220°	May-14
TRBDD04	735918	7172548	577m	45.1m	-60°	220°	May-14
TRBDD05	735918	7172548	577m	62.9m	-50°	220°	May-14
TRBDD06	735920	7172551	577m	75.3m	-75°	146°	May-14
TRBDD07	734799	7172829	577m	480.1m	-70°	345°	May-14
TRBDD08	735899	7172547	577m	65.7m	-70°	215°	Jul-14
TRBDD09	735920	7172548	577m	50.9m	-70°	215°	Jul-14
TRBC063	734972	7172596	567m	120m	-70°	035°	Sep-14
TRBC064	735079	7172332	577m	90m	-60°	360°	Sep-14
TRBC065	735079	7172312	581m	96m	-60°	360°	Sep-14
TRBC066	735644	7172416	583m	78m	-60°	195°	Sep-14
TRBC067	735652	7172247	593m	198m	-90°	360°	Sep-14
TRBC068	736348	7172474	582m	102m	-60°	030°	Sep-14
TRBC069	736416	7172589	586m	102m	-60°	210°	Sep-14
TRBC070	735942	7172552	577m	71m	-60°	216°	Sep-14
TRBC071	735923	7172548	577m	63m	-60°	216°	Sep-14
TRBC072	735921	7172548	577m	72m	-70°	216°	Sep-14
TRBC073	735903	7172547	577m	60m	-60°	216°	Sep-14
TRBC074	735904	7172568	577m	84m	-60°	216°	Sep-14
TRBC075	735923	7172528	577m	84m	-60°	306°	Sep-14
TRBC076	735041	7172290	576m	114m	-60°	360°	Sep-14
TRBC077	735934	7172536	587m	124m	-90°	360°	Feb-15
TRBC078	735887	7172530	582m	304m	-90°	360°	Feb-15
TRBC079	735063	7172317	568m	100m	-60°	357°	Feb-15
TRBC080	735917	7172534	583m	120m	-90°	360°	Feb-15
TRBC081	735942	7172562	578m	150m	-60°	210°	Feb-15
TRBC082	735079	7172291	577m	110m	-60°	357°	Feb-15
TRBC083	735001	7172615	573m	50m	-60°	357°	Feb-15
TRBC084	735636	7172402	580m	40m	-60°	357°	Feb-15
TRBC085	735931	7172575	575m	166m	-60°	210°	Feb-15
TRBC086	736426	7172520	580m	160m	-60°	357°	Feb-15
TRBC087	735087	7172365	567m	100m	-90°	360°	Feb-15

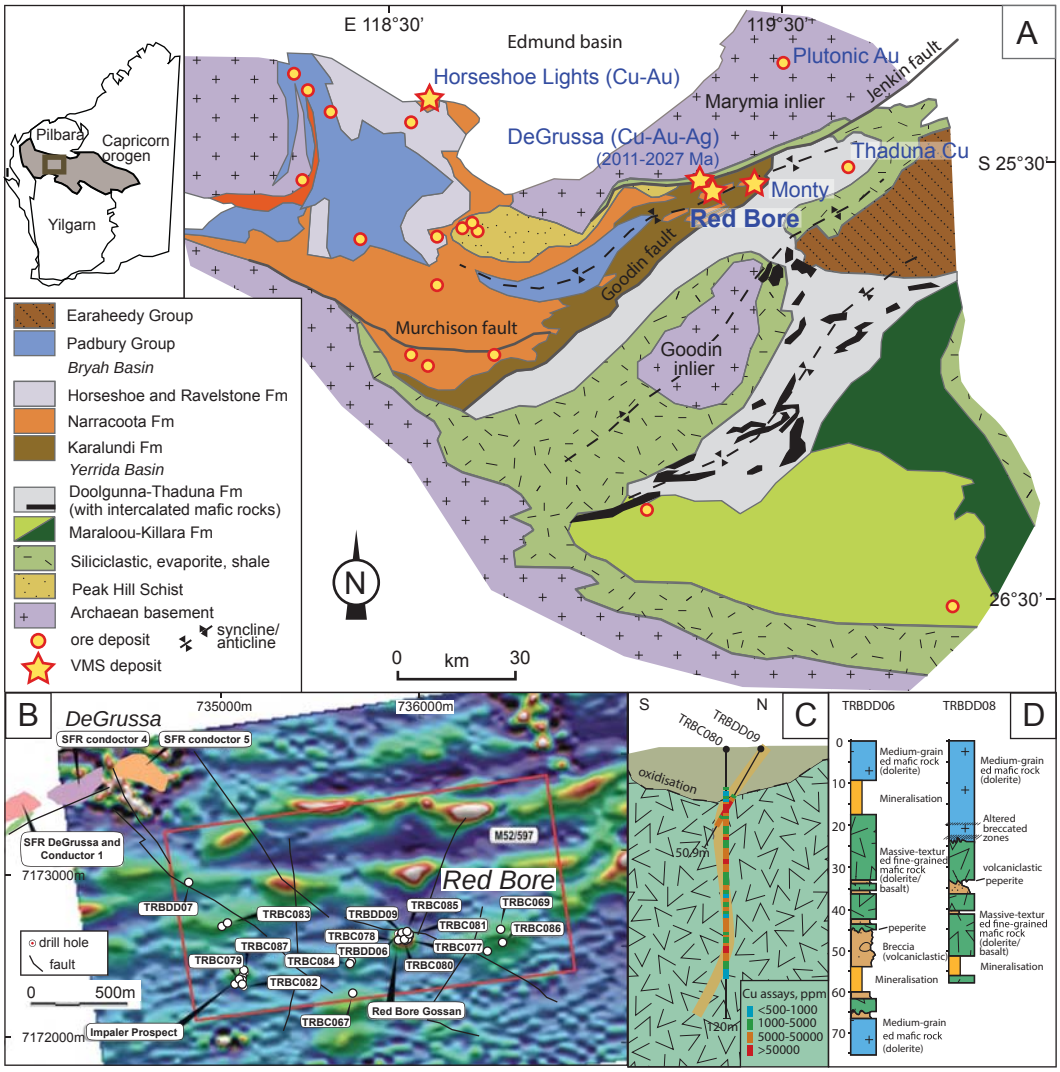
A
E 118°30'
119°30'
S 25°30'
26°30'
Edmund basin
Horseshoe Lights (Cu-Au)
Plutonic Au
Jenkin fault
Marymia inlier
DeGrussa (Cu-Au-Ag)
(2011-2027 Ma)
Thaduna Cu
Monty
Red Bore
Goodin fault
Murchison fault
Goodin inlier
Pilbara
Capricorn orogen
Yilgarn
Earaheedy Group
Padbury Group
Bryah Basin
Horseshoe and Ravelstone Fm
Narracoota Fm
Karalundi Fm
Yerrida Basin
Doolgunna-Thaduna Fm (with intercalated mafic rocks)
Maraloou-Killara Fm
Siliciclastic, evaporite, shale
Peak Hill Schist
Archaean basement
ore deposit
VMS deposit
syncline/ anticline
N
0 km 30
B
DeGrussa
735000m
736000m
SFR condoctor 4
SFR condoctor 5
SFR DeGrussa and Conductor 1
7173000m
7172000m
M52/597
Red Bore
TRBDD07
TRBC083
TRBDD09
TRBC085
TRBC069
TRBC081
TRBC086
TRBC078
TRBDD06
TRBC077
TRBC087
TRBC079
TRBC084
TRBC080
TRBC082
TRBC067
Red Bore Gossan
Impaler Prospect
drill hole
fault
0 500m
C
S
N
TRBC080
TRBDD09
oxidisation
50.9m
120m
Cu assays, ppm
<500-1000
1000-5000
5000-50000
>50000
D
TRBDD06
TRBDD08
0
10
20
30
40
50
60
70
Medium-grained mafic rock (dolerite)
Mineralisation
Massive-textured fine-grained mafic rock (dolerite/ basalt)
peperite
Breccia (volcaniclastic)
Altered breccated zones
volcaniclastic peperite

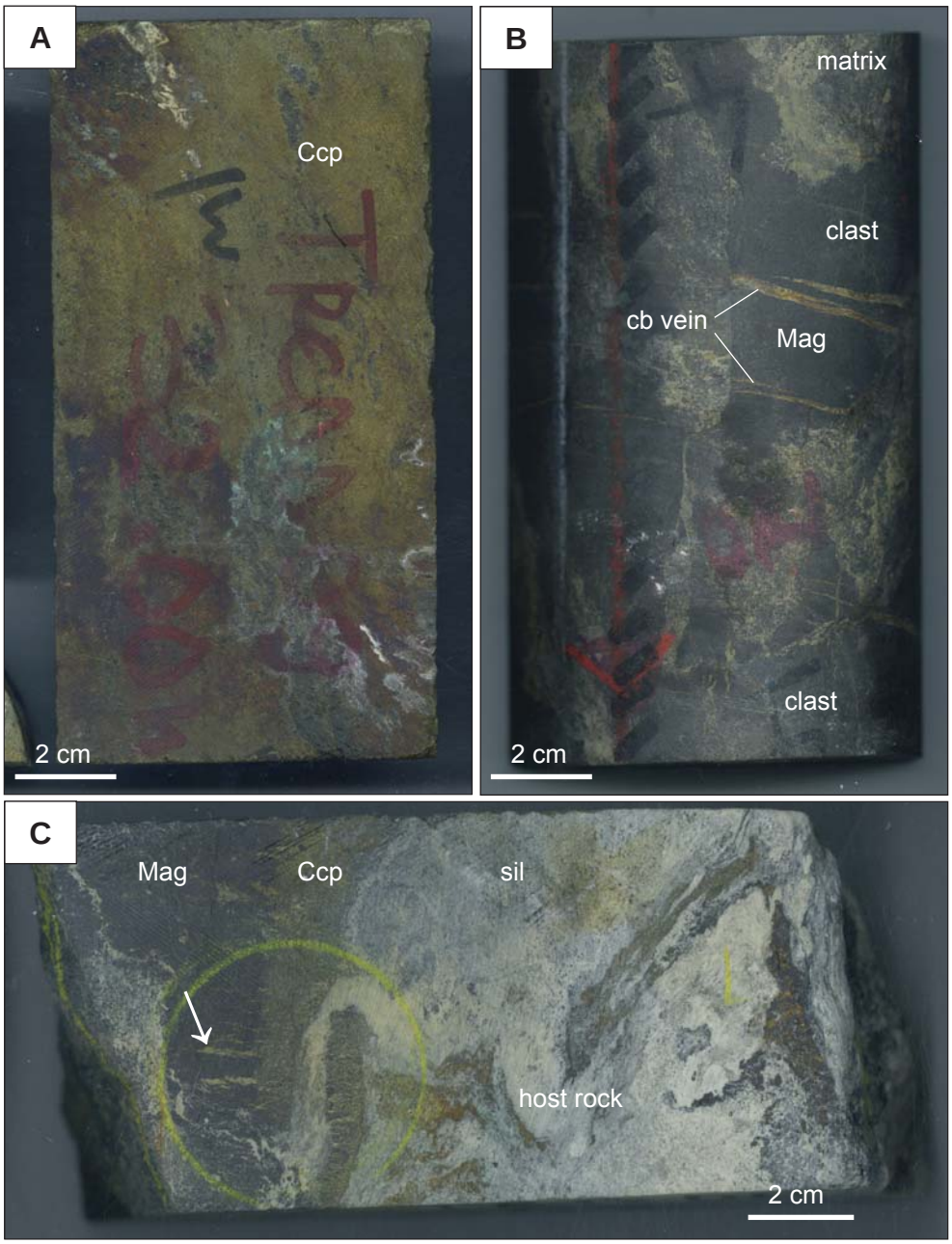

Fig. 2 Drill core samples from Red Bore. A Massive chalcopyrite, sample TRCDD09 32.0m. B Massive magnetite breccia. Clasts are cross-cut by carbonate (cb) veinlets. C external contact pf the ore body. Chalcopyrite (Ccp) truncates magnetite (Mag)

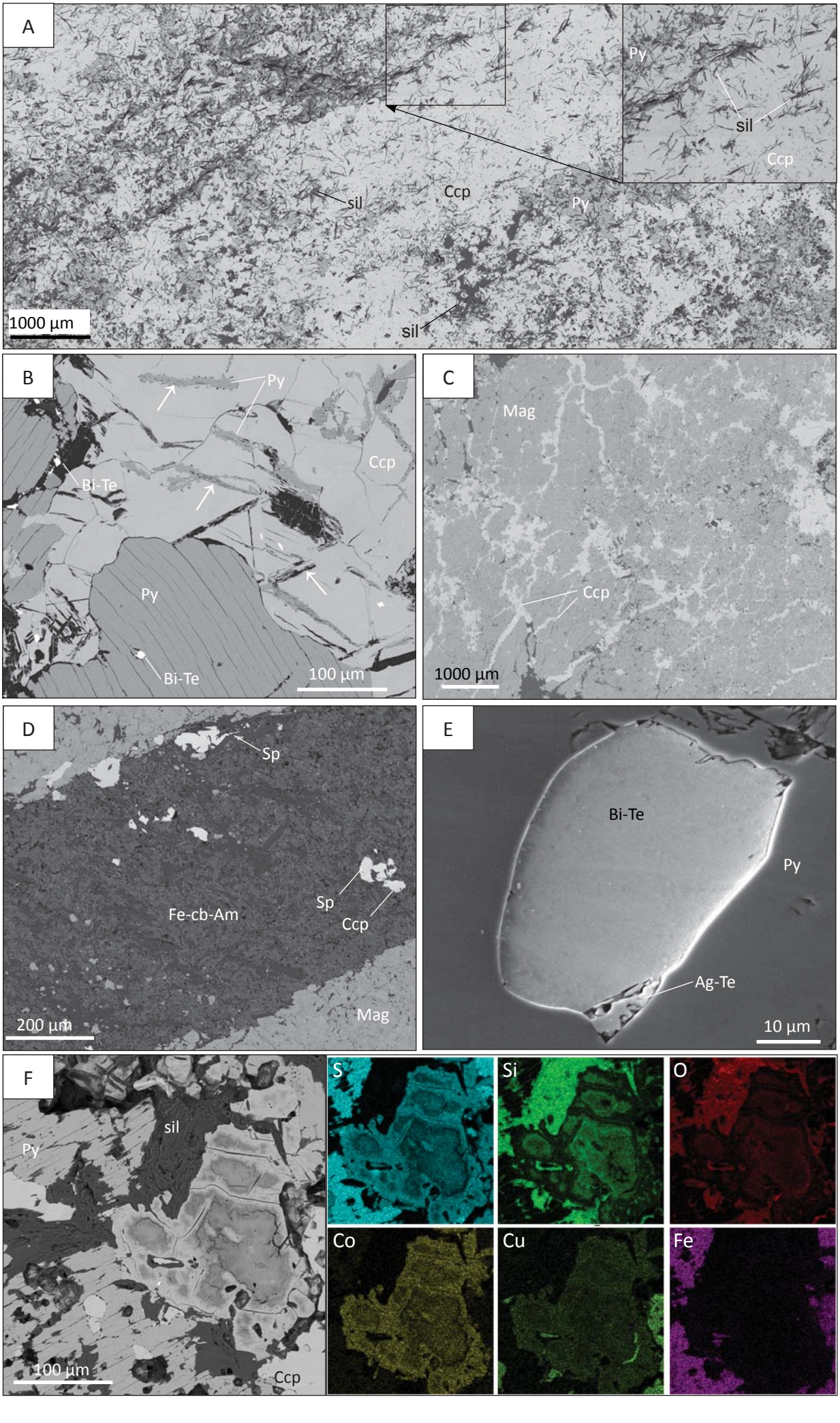
A
Py
sil
Ccp
sil
Ccp
Py
sil
1000 µm
B
Py
Ccp
Bi-Te
Py
Bi-Te
100 µm
C
Mag
Ccp
1000 µm
D
Sp
Sp
Ccp
Fe-cb-Am
Mag
200 µm
E
Bi-Te
Py
Ag-Te
10 µm
F
sil
Py
100 µm
Ccp
S
Si
O
Co
Cu
Fe

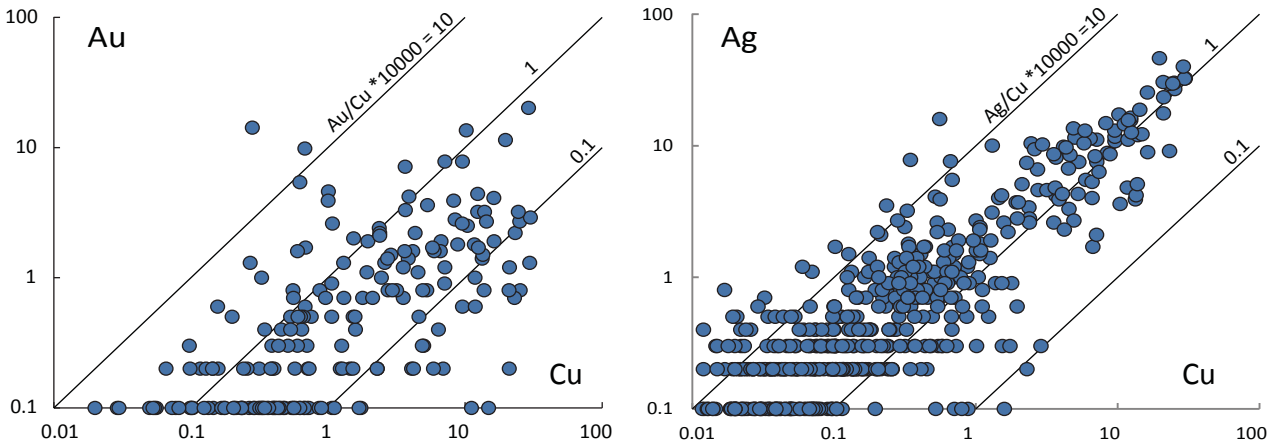

Fig 4 Bulk rock assays of Red Bore samples. Au and Ag as ppm, Cu as wt.%

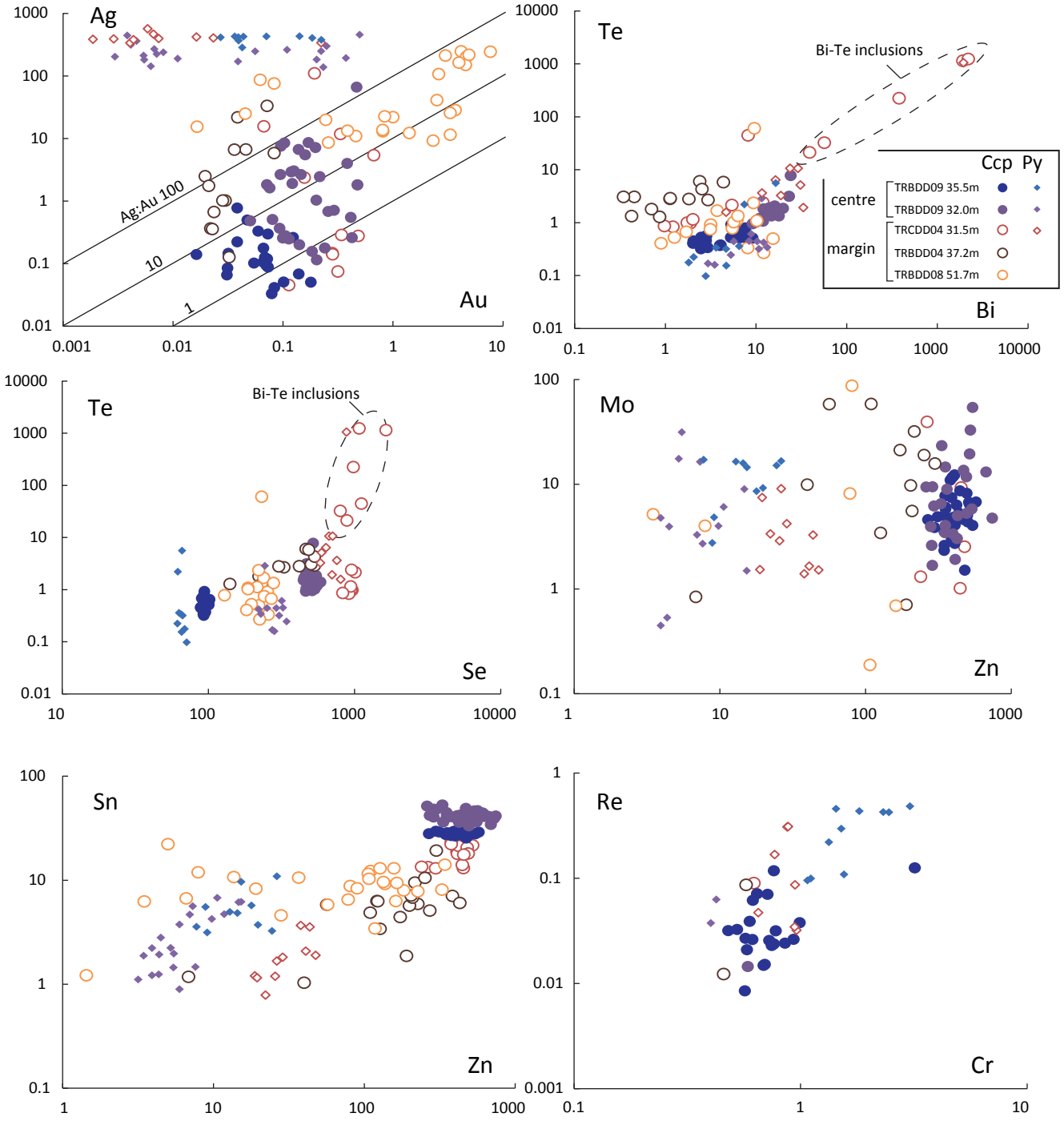

Fig 5 Trace element compositions of chalcopyrite and pyrite from Red Bore (LA-ICP-MS, all compositions as ppm). Samples from the centre (massive chalopyrite) and the margin of the deposit are distinguished

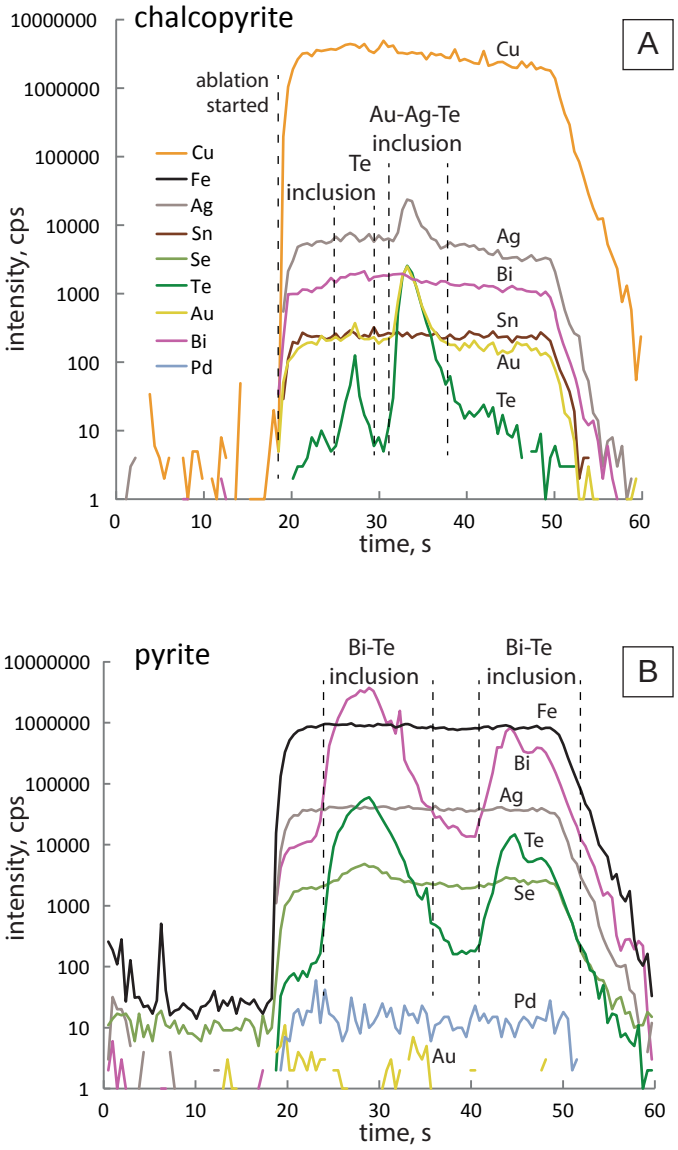

Fig 6 Laser ablation signal as counts per second (cps) of chalcopyrite (A) and pyrite (B) plotted versus time. Co-occurrence of element peaks indicates the presence of Te-Au-Ag and Bi-Te inclusions. A total Au = 7.7 ppm (A), sample TRBDD08 51.7m; B total Au = 0.02 ppm, sample TRCDD09 31.5m

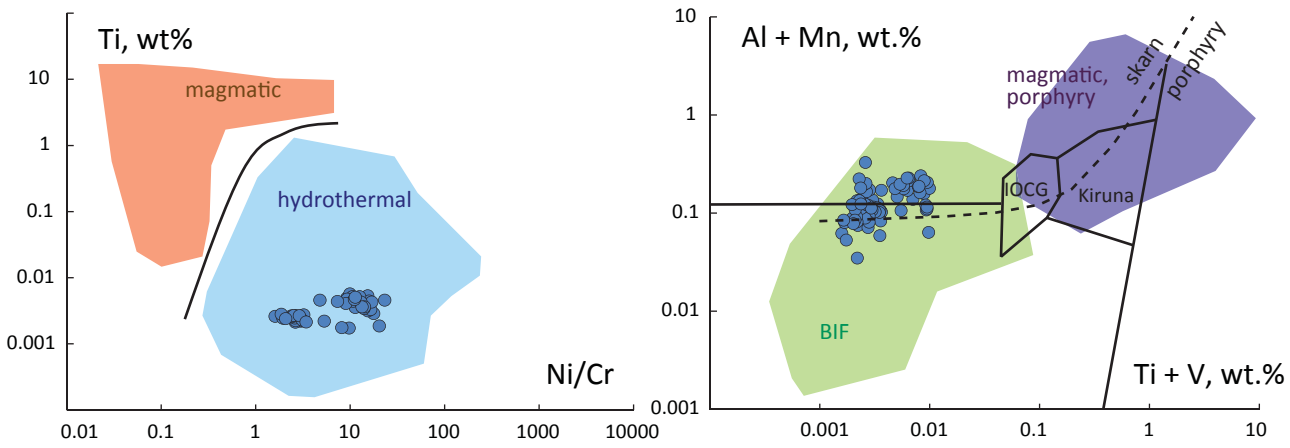

Fig 7 Trace element composition of magnetite from Red Bore (LA-ICP-MS). Classification from Nadoll 2014 and Dare 2014

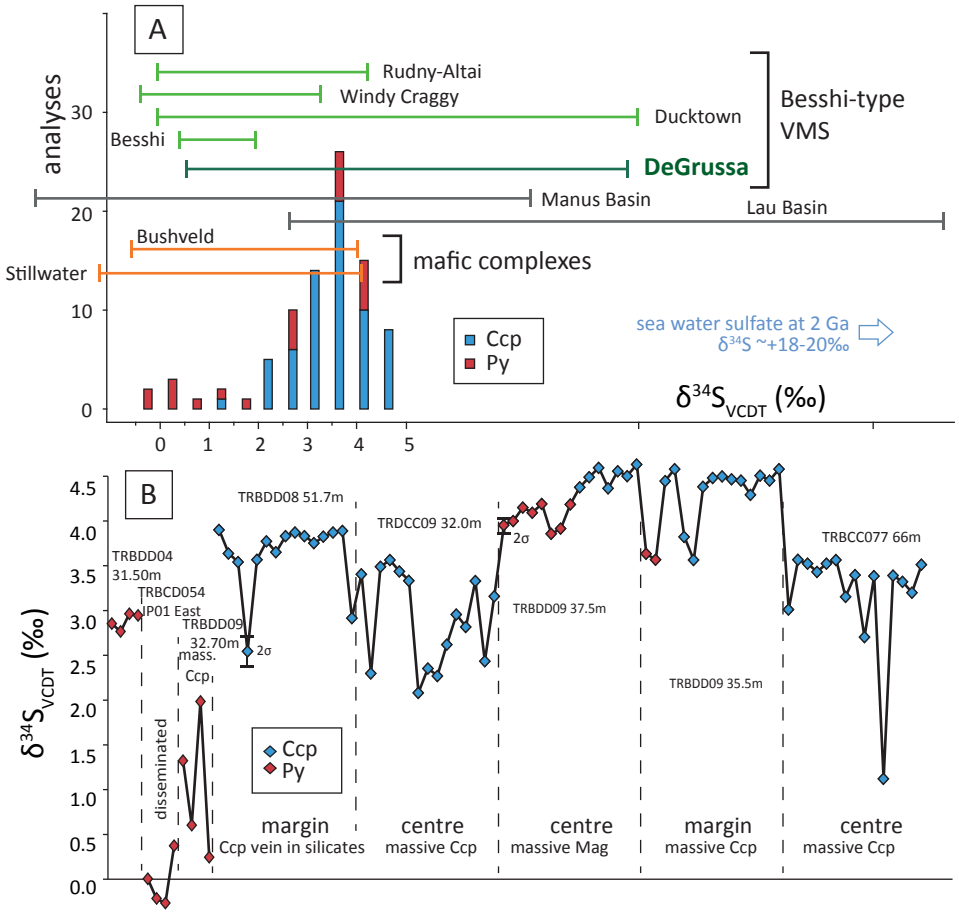

Fig 8 S isotope sulfide compositions at Red Bore (SIMS). **A** histogram, **B** plots of single analyses distinguished by sample and mineral phase. Abbreviations: Ccp chalcopyrite, Py pyrite. Ranges of d34S for sulfides from other VMS deposits and S-poor Bushveld complex (from Ripley and Li, 2003) are shown for comparison. Sea water sulfide composition from Farquhar et al. 2010

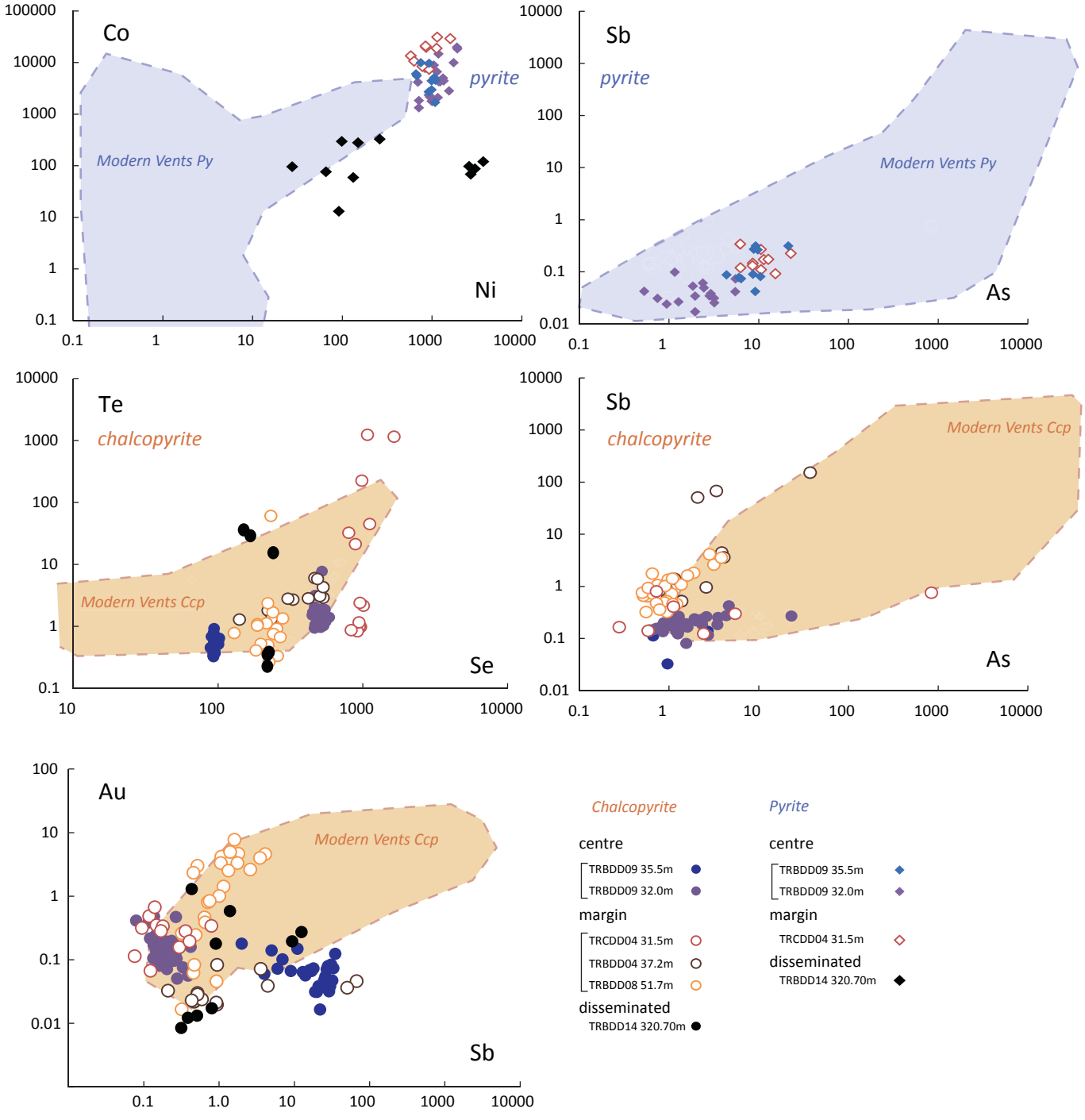

Fig 9 Composition of pyrite from Red Bore (LA-ICP-MS, all compositions as ppm) and spatially-associated VMS deposits (DeGrussa and Horseshoe Lights; Belousov et al., in review) compared with pyrite from modern submarine vents (Wholgemuth-Ueberwasser et al 2015; Keith et al 2016)

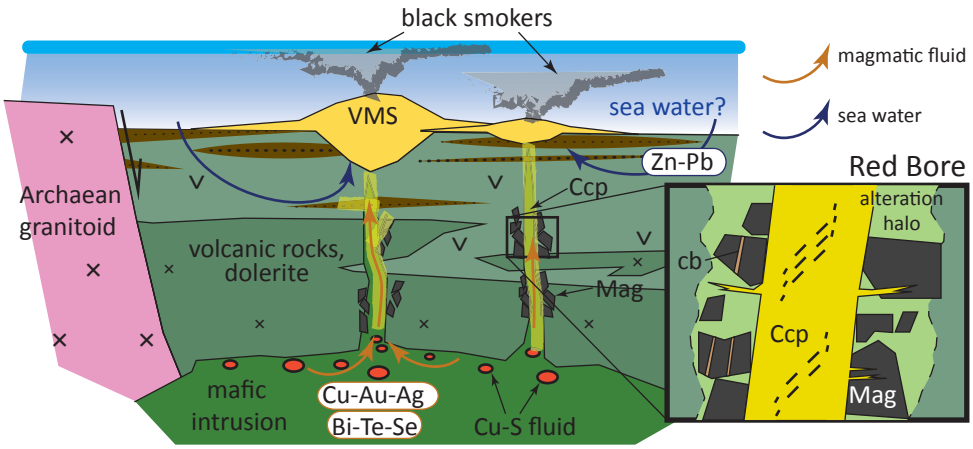

Fig 10 Genetic model for the formation of Red Bore mineralised pipes and co-genetic VMS deposits at DeGrussa. Cu, Au, Ag, Bi and other metals were likely transported from a magmatic fluid phase and fed into VMS deposits at the surface, where they would have mixed with sea water-derived fluids. Other elements, such as Zn, are found in VMS deposits but are depleted at Red Bore and may have been derived from leaching of the volcano-sedimentary pile by sea water fluids